University of Alberta

MULTI-LAYER BIOCHIP WITH INTEGRATED HOLLOW WAVEGUIDES

by

Dean Sheldon Spicer ©

A thesis submitted to the Faculty of Graduate Studies and Research in partial fulfillment of the requirements for the degree of **Master of Science**.

Department of Electrical and Computer Engineering

Edmonton, Alberta
Fall 2005

Library and
Archives Canada

Published Heritage
Branch

395 Wellington Street
Ottawa ON K1A 0N4
Canada

Bibliothèque et
Archives Canada

Direction du
Patrimoine de l'édition

395, rue Wellington
Ottawa ON K1A 0N4
Canada

Your file Votre référence
ISBN: 0-494-09293-9
Our file Notre référence
ISBN: 0-494-09293-9

NOTICE:
The author has granted a non-exclusive license allowing Library and Archives Canada to reproduce, publish, archive, preserve, conserve, communicate to the public by telecommunication or on the Internet, loan, distribute and sell theses worldwide, for commercial or non-commercial purposes, in microform, paper, electronic and/or any other formats.

The author retains copyright ownership and moral rights in this thesis. Neither the thesis nor substantial extracts from it may be printed or otherwise reproduced without the author's permission.

AVIS:
L'auteur a accordé une licence non exclusive permettant à la Bibliothèque et Archives Canada de reproduire, publier, archiver, sauvegarder, conserver, transmettre au public par télécommunication ou par l'Internet, prêter, distribuer et vendre des thèses partout dans le monde, à des fins commerciales ou autres, sur support microforme, papier, électronique et/ou autres formats.

L'auteur conserve la propriété du droit d'auteur et des droits moraux qui protège cette thèse. Ni la thèse ni des extraits substantiels de celle-ci ne doivent être imprimés ou autrement reproduits sans son autorisation.

In compliance with the Canadian Privacy Act some supporting forms may have been removed from this thesis.

While these forms may be included in the document page count, their removal does not represent any loss of content from the thesis.

Conformément à la loi canadienne sur la protection de la vie privée, quelques formulaires secondaires ont été enlevés de cette thèse.

Bien que ces formulaires aient inclus dans la pagination, il n'y aura aucun contenu manquant.

Canada

Reproduced with permission of the copyright owner. Further reproduction prohibited without permission.

University of Alberta

Library Release Form

Name of Author: Dean Sheldon Spicer

Title of Thesis: Multi-Layer Biochip with Integrated Hollow Waveguides

Degree: Master of Science

Year this Degree Granted: 2005

Dean Sheldon Spicer

Date: Sept. 6, 2005

For Alanna, Graham and the next little one

Abstract

The design and fabrication of a multi-layer microfluidic chip with integrated optics has been realized. The lower layer of the chip is made of silicon and provides the optical functionality of the device. Light guiding between the edge of the chip and the area of interest is achieved by metalized hollow v-groove waveguides fabricated by anisotropic silicon etching. Interfaces between the fluidic and optical layers are provided by the reflective Si (111) end facets of the waveguides. Bonded to the silicon layer is a pyrex upper layer which caps the waveguides and contains etched fluidic microchannels. Fabricated chips were able to successfully guide light between the edge of the chip and the area of interest. The hollow waveguides were used both to guide excitation light as well as collect fluorescence emitted from microparticles. Chip designs intended for capillary electrophoresis, and polymerase chain reaction have been fabricated.

Acknowledgements

I would like to express my thanks and appreciation to my supervisor, Dr. McMullin, who gave me the direction and resources to pursue work in this field. I also extended my gratitude to Dr. Vien Van and Dr. Subir Battacharjee for being on my committee.

During the course of this work many individuals came along side me with their expertise for which I am extremely grateful. In particular, Holly Rourke for many fabrication tips and consultation during the initial process design. Also, her colleagues at Norcada, Dr. Yuebin Ning and Mike Colgan for helpful advice during the fabrication stage of my project. I would also like to thank Thomas Clement who helped me at several key moments throughout this project in aspects of both fabrication and testing. I also extend my thanks to TRLabs and Dave Clegg in particular who allowed me access to their equipment for some aspects of the testing.

I am grateful to the University of Alberta Nanofabrication (NanoFab) staff, in particular, Dr. Ken Westra, Shane McColman, Aruna Kroech, Dione Chambers and Stephanie Bozic for their advice and training which enabled a rewarding fabrication aspect of this project.

I would like to thank the Natural Sciences and Engineering Research Council of Canada (NSERC) and the Canadian Institute for Photonic Innovation (CIPI) for financial support, as well as Micralyne Inc. of Edmonton for their in-kind contribution to this project.

Finally, my most grateful thanks go to my wife Alanna and son Graham, who walked with me on this long road. I also thank my family who supported and encouraged me during this time.

Contents

List of Tables

List of Figures

List of Symbols

Ag	silver
APD	avalanche photo diode
Au	gold
BOE	buffered oxide etch
CE	capillary electrophoresis
Cr	chrome
dB	decibel
DI	deionized
EDP	ethylenediamine pyrocatechol
EDW	ethylenediamine pyrocatechol with water
GUI	graphical user interface
HF	hydrofluoric acid
Hz	hertz
HMDS	hexamethyldisilazane
IPA	isopropyl alcohol
KOH	potassium hydroxide
LPCVD	low pressure chemical vapor deposition
mTorr	millitorr
NA	numerical aperture
NOA	Norland optical adhesive
PCR	polymerase chain reaction
PDL	polarization dependent loss
PDMS	polydimethylsiloxane
PMT	photomultiplier tube
Pt	platinum
RIE	reactive ion etching

RT-PCR	real time polymerase chain reaction
sccm	standard cubic centimeters per minute
SG	specific gravity
Si	silicon
SiO_2	silicon dioxide
SiN_2	silicon nitride
SNR	signal to noise ratio
TE	transverse electric
Ti	titanium
TM	transverse magnetic
UV	ultraviolet
VASE	variable angle spectroscopic ellipsometer
W	watt
μm	micrometer

Chapter 1

Introduction

1.1 Lab-on-a-Chip

Initially, the concept behind microfluidics or lab-on-a-chip was put forward by H. M. Widmer [1] in 1983 as what he saw was needed by analytical chemists for improved instrumentation.

> *"an integrated, analytical system, combining all the sequential steps of analysis in a single, on-line system. This would link together sampling, sample preparation, cleanup procedures, derivatisation steps, enrichment of trace components, separation, qualitative determination (including identification or speciation) and structure elucidation, quantitative analysis of constituents, output and listing of results (documentation), signal processing for further use (e.g. in process steering) and final problem solution. Such an integrated, total analysis system would operate automatically..."*

In a truly innovative paper in 1990 by Manz [2], Widmer's vision was expanded with a look at the theoretical viability of a micro total analysis system (μTAS) and its possible enabling technologies. Since it's initial conception, the principles behind μTAS have been accepted by other fields of research and broader terms like microfluidics and lab-on-a-chip have become more popular for describing the original μTAS concept.

Current lab-on-a-chip technology is still a long way from Widmer's original vision, but significant advances have been made. Examples of applications where microfluidic devices are being developed include: genomics and proteomics (PCR, RT-PCR) [3, 4, 5], pathogen detection [6], environmental testing [7], analysis of bodily fluids [8] and cell counting and sorting [9], biosensors and tools for biochemistry [10]. Miniaturization of devices that perform these tasks leads to decreased sample volumes needed, less reagents consumed, faster analyses and of course portability.

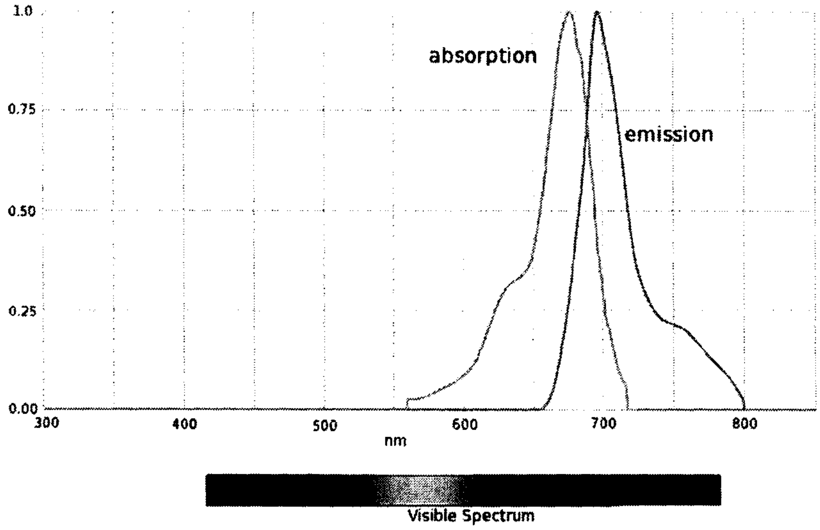

Figure 1.1: Example absorption and fluorescence emission spectra

For more reading on the current state of microfluidic technology, see comprehensive reviews [11, 12], as well as journals such as *Lab on a Chip* [13], *Journal of Micromechanics and Microengineering* [14], *Electrophoresis* [15], and *Analytical Chemistry* [16]. According to Kamholz [17], the amount of literature on microfluidics is growing rapidly. In 1999, there were only 75 publications on microfluidics. Four years later, in 2003, there were about 580 publications dealing with microfluidics.

1.1.1 Fluorescence Detection

Microfluidic applications often use fluorescence detection to quantify the results of an on-chip reaction. Fluorescent molecules act as molecular tags that label molecules of particular interest. A molecule is said to fluoresce when it absorbs light of one wavelength and emits light of another (longer) wavelength. The mechanism behind this effect is the radiative relaxation of an electron from an excited state. The electron is excited by the energy from the incident light at the shorter wavelength, and then radiates light at a longer wavelength as it relaxes. See Fig. 1.1 for typical absorption and emission spectra [18].

A fluorescent molecule becomes useful when we can selectively attach it to another molecule that we are interested in. As an example, real-time polymerase chain reactions (RT-PCR) are often done with intercalating fluorescent dyes in order to quantify the amount of product as the reaction proceeds. An intercalating dye is a molecule that incorporates between double strands of DNA as

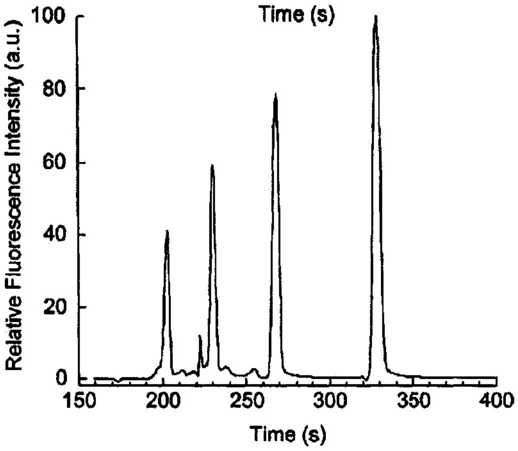

Figure 1.2: Typical CE Electropherogram

they are being amplified. As more intercalating dye is incorporated into the amplified DNA strands, the fluorescence signal from the reaction product will increase [19]. In this case, the increase of fluorescence (or lack thereof) is the result we are looking for from the analysis.

Capillary electrophoresis (CE) is another example of a process that uses fluorescence to determine the results of the procedure. In a CE analysis, pieces of DNA which have been labelled by with a fluorescent tag are driven down a channel filled with gel using a high voltage. The pieces of DNA separate by size as they travel down the channel. At a specific point near the end of the channel, a laser is used to excite fluorescence in the fluorescent tag attached to the DNA fragments as they pass by. Smaller DNA fragments will cross the detection point sooner than larger fragments. By noting the signal strengths from the different bands created by the passing sample, the relative concentrations of the different DNA fragments can be determined. An example graph of what this analyses might look like is shown in Fig. 1.2 (taken from [20]).

The instrumentation required to do the fluorescent excitation and collection is quite bulky. An example of such an instrument is the epiluminescent confocal microscope that is included in the microfluidic toolkit sold by Micralyne [21]. The actual microfluidic chip is quite small, but the entire system to do the analysis is still very bulky. See Fig. 1.3 [21] for an illustration. It is the goal of this work to eliminate bulky optical instrumentation by integrating the optics onto the microfluidic chip.

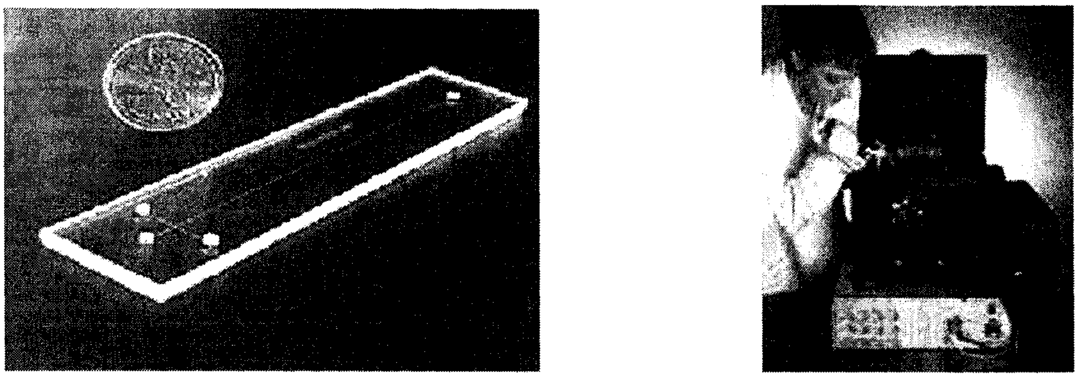

(a) Microfluidic chip typically used for capillary electrophoresis

(b) Microfluidic toolkit capable of performing capillary electrophoresis and laser induced fluorescence detection

Figure 1.3: Fluorescent detection instrumentation.

1.2 Biochips with Integrated Optics

There are two functions performed by the optical system, excitation of the sample, and collection of the resulting fluorescence. If either (or both) of these functions could be done by integrated optics, the need for a bulky lens based system could be significantly reduced or even eliminated.

There are many different methods of integrating microfluidics with optics. Past work in our lab includes silver doped ion-exchange waveguides integrated with microfluidics [22]. These waveguides were used to deliver light to the fluidic microchannels as a means of exciting a fluorescent dye. Another approach to integrating optics is by direct laser writing in curable UV epoxies [23]. A computer controlled system developed in our lab is able to write lines in UV curable epoxy that can be used to guide light once the uncured epoxy is rinsed away. Microfluidic channels were also fabricated by defining the walls of the channels with cured epoxy lines and then capping the structure with a glass slide. Mogensen et al. [24] fabricated a chemical absorption cell device from patterned polymer waveguides and microfluidic channels in SU-8. This same group also developed silica on silicon waveguides and successfully integrated them with microfluidics [25, 26, 27].

The recent use of polydimethylsiloxane (PDMS) as a material for microfluidic devices [28, 29] has led researchers to find a way of combining fluidics formed in PDMS with waveguide structures. To this end, some have tried embedding optical fibre by casting PDMS directly over top of a carefully positioned fibre [20]. Others have tried hollow waveguides in PDMS as a way of delivering and collecting light in an on-chip absorption device [30].

1.3 Overview of this Research

As microfluidic systems become more complex, the ability to fabricate multilayer systems becomes appealing. Additional layers can contain additional fluidics [31, 32] or even an altogether different functionality. Quake et al. [33] have used multiple layers to construct a device with pneumatic valves and pumps. Daridon et al. [34] fabricated a multi-layer glass chip with an optical cuvette between two fluidic layers meant for absorption measurements. This same group constructed a multilayer system for fluorescence detection that used microlenses and a chrome mask layer as a spatial filter to reduce noise due to excitation light entering the detector [35, 36].

In this work, the optical and fluidic functionality are in separate layers. Using multiple layers for a biochip with integrated optics allows for optimization of each aspect separately. Once the fluidics and integrated optics are optimized they can be bonded together to form the complete device. The method of optical integration in this work is by hollow v-groove waveguides, fabricated by anisotropic silicon etching. This is a continuation of previous work done on hollow v-groove waveguides [37]. The idea was extended by envisioning a silicon (111) end facet as a mirror that could redirect light upward out of the plane of the waveguide. When considering a microfluidic system, this can be used to direct light to a fluidic layer above the end facet. In a multilevel biochip, this end facet serves as an interconnect between the two functional layers, optical and fluidic. A silicon (111) end facet is shown in Fig. 1.4.

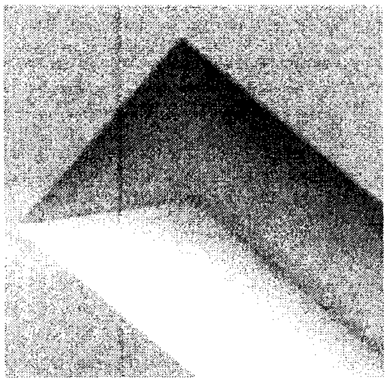

Figure 1.4: Silicon (111) end facet

Using silicon end facets as mirrors is not novel, as it has been reported in the literature [38, 39, 40]. Strandman et al. [39] used the (111) end facet to redirect light from a fibre upwards into a

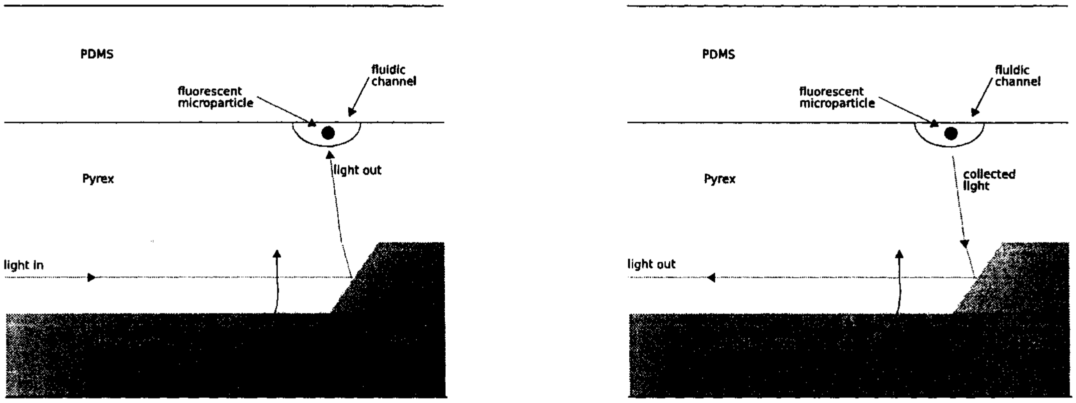

(a) excitation

(b) collection

Figure 1.5: Device concept

photodetector for a optical input-output coupler. Tiggelaar et al. [40] used silicon end facets to couple light on and off a microfluidic chip designed for detection of ammonia.

The final device concept is shown in Fig. 1.5. The optics are fabricated by anisotropic etching of the silicon. V-grooves were formed by the (111) planes with the end facet positioned under the fluidic channels. The v-grooves were coated with metal and capped so that they could be used as hollow waveguides. Fluidic channels are created by etching trenches in the pyrex component. The fluidic channels are capped with a superstrate of polydimethylsiloxane (PDMS) that provides a lid for the fluidic channels and can be easily punched with access ports for allowing fluid on and off the chip. The PDMS layer is easily removed as it forms a reversible bond with the pyrex. Since the PDMS layer is removable, the finished device is reusable and easy to clean.

The remainder of this thesis details the theory, fabrication and experimental work done with the fabricated devices described herein. Chapter 2 presents the relevant theory for hollow waveguides as well as the simulation work done to predict their performance. Chapter 3 outlines the design and fabrication of the devices. Significant process steps and relevant theory are also presented when appropriate. A complete step-by-step fabrication process can be found in Appendix B. Chapter 4 details the experimental work done with the fabricated chips. Optical performance is characterized and compared with simulated predictions from Chapter 2. The results of fluorescence experiments using the v-grooves in both the excitation and collection configurations are presented. Chapter 5 summarizes the accomplishments of this work and discusses directions for future work.

Chapter 2

Hollow Waveguide Theory and Simulation

2.1 Waveguide Theory

An optical waveguide can be broadly defined as a structure that confines light and directs it without the use of refocusing optics like lenses and mirrors. The most popular type of waveguide is the dielectric waveguide often used in fibre optic communication systems.

2.1.1 Dielectric Waveguides

A dielectric waveguide is made of a low loss core material surrounded by another material, the cladding, of lower index of refraction. The difference in refractive indices between the core material and the cladding confines the light by total internal reflection.

When light strikes an interface, the angle of the refracted light can be calculated by Snell's law which is shown in Eq. 2.1. The angle of the reflected light is always equal to the angle of the incidence ($\theta_1 = \theta_3$) as defined in Fig. 2.1.

$$n_1 \sin\theta_1 = n_2 \sin\theta_2 \tag{2.1}$$

There is an angle, known as the critical angle, for which the refracted light will be 90° to the normal. When the angle of an incident light ray is greater than this critical angle, it will be totally reflected. This principle is illustrated in Fig. 2.1. The critical angle can be calculated using Eq. 2.2.

$$\theta_c = \arcsin\left(\frac{n_2}{n_1}\right) \tag{2.2}$$

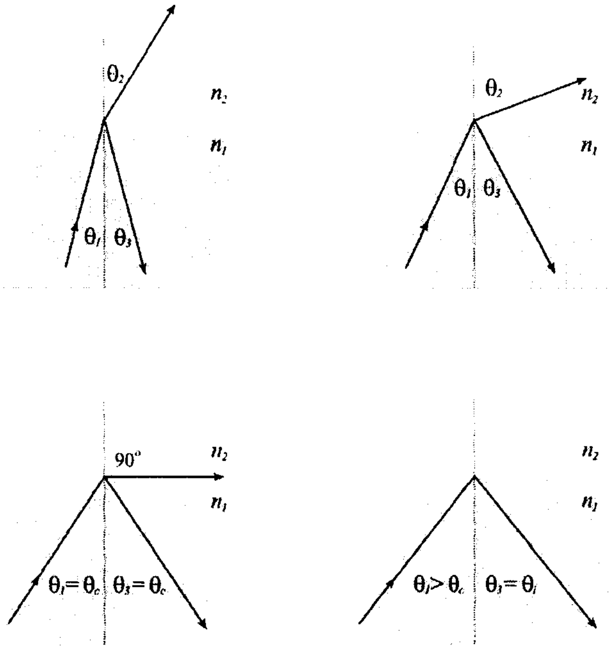

Figure 2.1: Snell's law and the critical angle

where θ_c is the critical angle, and n_1 and n_2 are the index of the refraction of the material on the incident and transmitted side of the interface respectively.

Since the reflections are complete (lossless), the loss mechanism in total internal reflection waveguides is due to the absorption of the propagation material, not the internal reflections.

2.1.2 Leaky Waveguides

There is another type of waveguide that does not use total internal reflection to confine light to a region of higher index of refraction. Instead, light is confined to a region of lower index of refraction by highly reflective surfaces. This type of waveguide is known as a 'leaky' waveguide. A leaky waveguide does not support any guided modes in the same sense as a dielectric waveguide. The light is guided simply by reflections off of the surrounding medium. Performance of leaky waveguides is dominated by the efficiency of these reflections, not by the absorption loss of propagation medium. Leaky waveguides typically use a metal film or an antiresonance coating as the reflective cladding. Leaky waveguides that use an antiresonance coating are known as ARROW waveguides [41, 42]. The efficiency of ARROW waveguides is usually higher than waveguides made with a metal film at the expensive of ease of fabrication. Hollow waveguides are those which utilize air as their core

(a) structure of dielectric waveguide

(b) structure of leaky waveguide

Figure 2.2: Comparison of waveguide structures

material, and are typically a subset of leaky waveguides. It should be noted that it is theoretically possible to surround air with a material of lower index of refraction [43].

Hollow leaky waveguides have some commercial interest due to their ability to transmit wavelengths far into the infrared (even below 20 μm). Since the core of a hollow waveguide is air, they are able to handle very high power (hundreds of watts). The most common use of these waveguides is the delivery of high power laser radiation for medical and industry applications (metal cutting and surgery) [44, 45].

2.1.2.1 Reflection at an Interface

Since the performance of a hollow leaky waveguide is determined by the reflections at the cladding, an understanding of the theory behind the reflection and refraction of light at an interface is essential.

Consider the reflection shown in Fig. 2.3 (taken from [46]). A ray is propagating in medium one, and strikes medium two with a particular angle relative to the interface normal. As mentioned in the previous section, the angle of the reflected ray is simply equal to the incident angle ($\theta_1 = \theta_3$), while the angle of the refracted ray can be determined by Snell's law [46] given in Eq. 2.1.

The efficiency of the reflection can be determined from Fresnel's equations [46] shown in Eq. 2.3 and 2.4, which give a relationship between the relative amplitude of the electric field that is reflected from a surface and the index of refraction of the material.

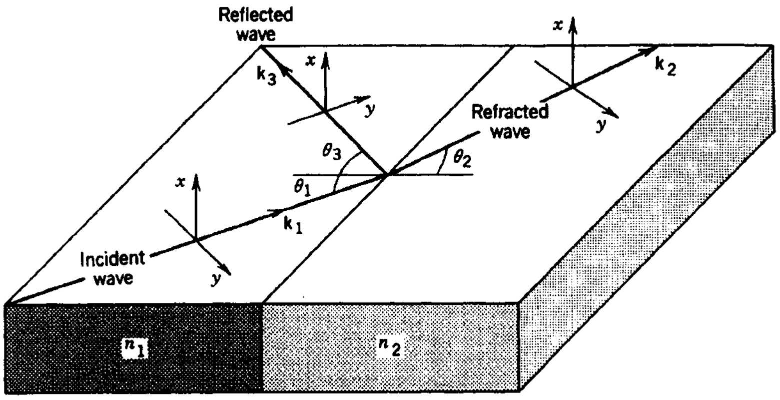

Figure 2.3: Reflection at an interface

$$r_x = \frac{n_1 \cos\theta_1 - n_2 \cos\theta_2}{n_1 \cos\theta_1 + n_2 \cos\theta_2} \tag{2.3}$$

$$r_y = \frac{n_2 \cos\theta_1 - n_1 \cos\theta_2}{n_2 \cos\theta_1 + n_1 \cos\theta_2} \tag{2.4}$$

where $\cos\theta_2$ can be rewritten in terms of θ_1 using Snell's law.

$$\cos\theta_2 = \left(1 - (\frac{n_1}{n_2})^2 \sin^2\theta_1\right)^{\frac{1}{2}} \tag{2.5}$$

It is important to notice that these equations also depend on the angle of the incident light. Fig. 2.4 shows the reflection coefficients for an air-glass interface at various incident angles calculated with Fresnel's equations. The reflectance, the power reflected from the interface, is given by the square of the reflection coefficient [46] as shown in Eq. 2.6.

$$R = |r|^2 \tag{2.6}$$

Fresnel's equations are most often applied to dielectrics, but they can also be applied to materials with absorbing properties if one takes the index of refraction to be complex [47]. Simply substituting $\tilde{n} = n - jk$ where n is the real part and k is the imaginary part of the index of refraction into equations 2.3 and 2.4 will yield the appropriate expressions. The real part of the index of refraction

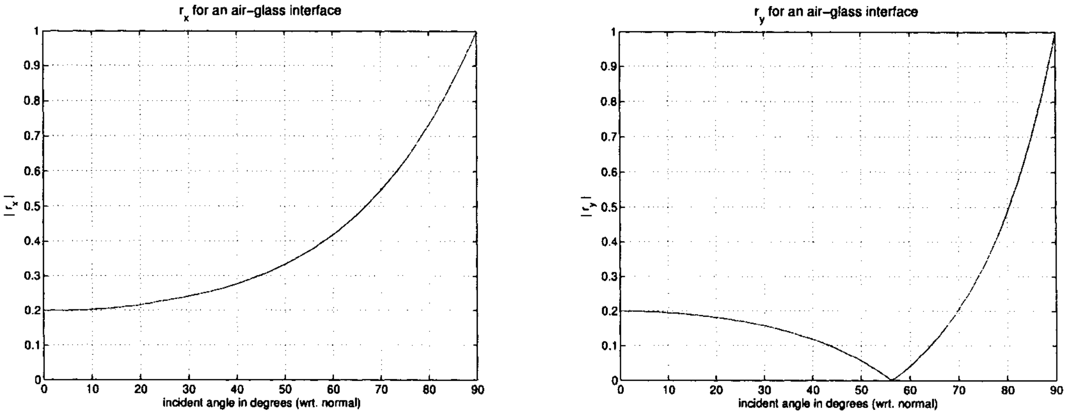

(a) Magnitude of the reflection coefficient in the x direction

(b) Magnitude of the reflection coefficient in the y direction

Figure 2.4: Fresnel reflection coefficients for an air-glass interface

is related to the speed of the electromagnetic wave as it travels through the medium by $n = c/v$ where c is the speed of light in a vacuum, and v is the speed of light in the medium. The imaginary part of the index of refraction, k, is known as the extinction coefficient and indicates how quickly the electromagnetic wave is damped as it passes through a medium. As light travels through an absorbing medium, its intensity decays according to $I(z) = I_o e^{-\alpha z}$ where α is the *absorption* coefficient (a different quantity than the previously mentioned *extinction* coefficient) and I_o is the intensity of the light just inside the material. The absorption coefficient is related to the extinction coefficient by $k = \frac{\lambda}{4\pi}\alpha$ [48, p 614].

Since the index of a refraction of a metal is complex ($k > 0$), the reflection coefficients are also complex. The reflectance (reflected power), is then calculated by multiplying the reflection coefficient by its complex conjugate.

$$R = r \cdot r^* \tag{2.7}$$

Therefore, the reflected power of a light ray incident on an interface is dependent on the angle of incidence as well as the properties of the material. In the case of a metal film (with complex index of refraction), both the real part of the index of refraction as well as the absorption of the material affect the magnitude of the reflected power.

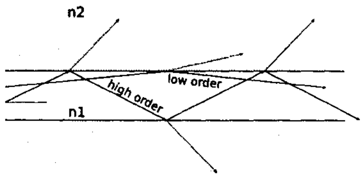

Figure 2.5: Hollow waveguide modes

2.1.2.2 Expected Loss in a Hollow Waveguide

In a hollow waveguide, the power as a function of distance along the guide will be determined by the reflection coefficient of the cladding material and the number of reflections per unit length that a ray undergoes. For any given ray with a particular launch angle, the power as a function of distance along the waveguide can be described as

$$P(z) = P_o R^{nz} \tag{2.8}$$

where P_o is the initial power in the ray, R is the reflectance (always ≤ 1), n is the number of reflections per unit length and z is the distance along the waveguide.

In a hollow waveguide, the ray angular distribution will narrow as it propagates. This is due to rays with higher launch angles being attenuated more quickly than rays with lower launch angles. Rays with higher angles are associated with waveguide modes of higher order [49]. In this discussion, rays with high launch angles will be referred to as a higher order mode. Similarly, rays with a lower launch angle are associated with a waveguide mode of lower order, see Fig. 2.5. The reason for this narrowing of angular distribution is due to two effects. First, the higher order rays undergo more reflections per unit length of the waveguide than the lower order rays. Since each reflection causes loss, this attenuates the ray. Also, a higher order ray sees the reflections at reduced efficiency due to the angular dependence of Fresnel's equations. See Fig. 2.4 for an example reflection coefficient curve. Rays with angle significantly different from glancing angles see a much lower reflection coefficient. This also increases the loss per unit length for that ray.

It has been shown that when a hollow waveguide is used to guide light that has been launched from a fibre, it decays according to Eq. 2.9 [37].

$$P(z) = \frac{P_o}{(1 + \alpha z)} \tag{2.9}$$

2.2 Simulation

In order to better understand the capabilities of the proposed microfluidic chip with integrated hollow waveguides, numerical simulations were undertaken. Custom software, coded in MATLAB, used simple ray-tracing techniques to predict the behavior of the light in the waveguides. Since the dimensions of the waveguide are much larger than the wavelength of the light used, diffraction and interference effects were not considered in the model.

Waveguide structures were modelled as a collection of planes, each with an arbitrary refractive index. Rays were launched into the end of the waveguide with a starting coordinate, propagation vector and value for the optical power in two orthogonal polarizations, transverse electric (TE) and transverse magnetic (TM). The software model considers TE to be the polarization at the launch point with electric field vector that is in the y direction. Similarly, the orthogonal polarization TM, is defined to be the polarization that is in the x direction at the launch point. Fig. 2.6 shows the coordinate system for the waveguide simulations. It is a right handed system, with z being the propagation direction. The rays are tracked as they propagate down the waveguide losing power as they reflect off the planes that define the waveguide walls. Everytime a ray intersects a wall, the TE and TM components are expressed in terms of vectors that are perpendicular and parallel to the plane of incidence (refer to Fig. 2.3). Once decomposed, Fresnel's equations (Eq. 2.3 and 2.4) are used to calculate the power loss for each component. The resulting polarization vectors are then transformed back to the waveguide coordinate system and stored as TE and TM according to the initial definition.

Input rays are read in from a file which records the starting point (x,y,z), propagation vector (kx, ky, kz) and optical power in TE and TM (Pte, Ptm). This allows for different types of launching conditions to be used by simply generating a new input file. The output file contains the same information and is identical in format as the input file, enabling the output of one simulation to be used as the input to a subsequent simulation.

More detail on the usage of the simulation software can be found in Appendix A.

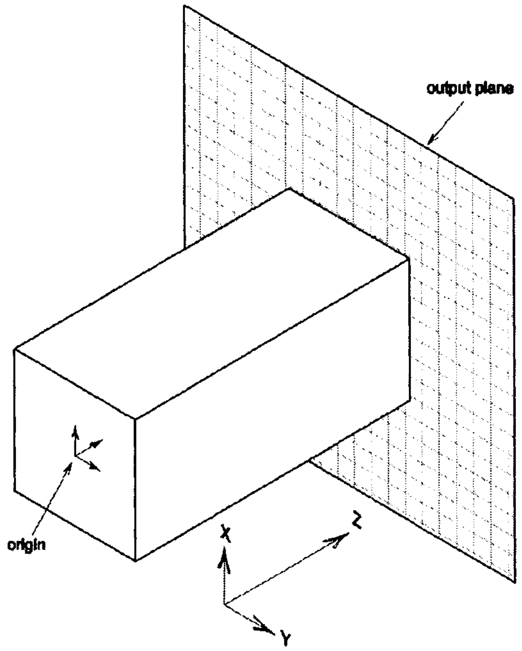

Figure 2.6: Waveguide coordinate system

2.2.1 Simulation Outputs

There are several types of output that can be generated from a simulation. The power distribution along the waveguide can be observed as crossections at specific z values, or it can be displayed as a side or top view. Also, as each ray reaches the output plane, its coordinates, propagation vector and power in TE and TM polarizations are recorded in a file. More detail on each simulation output and detail of any significant results attained are given in the following subsections.

2.2.1.1 Crossections

Crossections of the power along the waveguide can be plotted by recording the rays as they pass through a plane orthogonal to the waveguide. Every time a ray passes through a grid element, the power of the ray is added to the value of the element. In this way, a picture of the waveguide power at that crossection is constructed. Fig. 2.7 shows an 50 μm diameter input beam with an angular spread of 12 degrees expanding in a 400 μm wide v-groove waveguide.

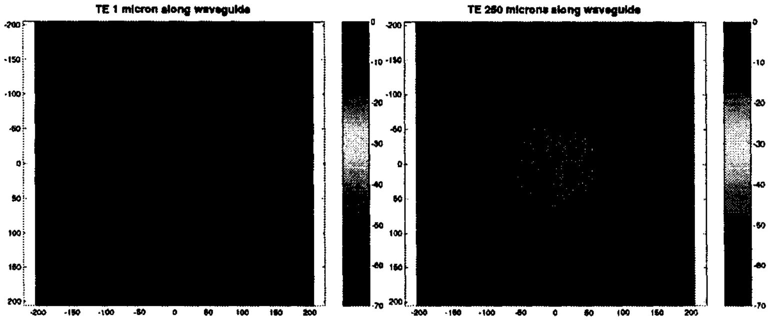

(a) z = 1 micron

(b) z = 250 microns

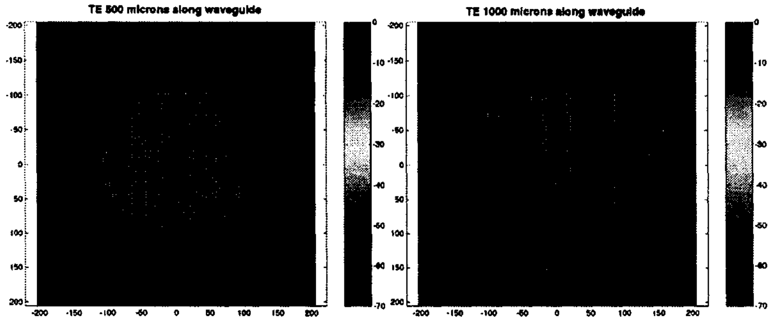

(c) z = 500 microns

(d) z = 1000 microns

Figure 2.7: Power distribution of the TE mode as it propagates along a 400 μm wide v-groove waveguide

2.2.1.2 Power Loss

Power distribution crossections also allow the calculation of power loss with distance along the waveguide. By summing all the power that remains inside the waveguide boundaries, a value for the power at a particular z value can be determined. In this way, the power remaining in the waveguide as a function of distance as shown in Fig. 2.8 can be constructed.

Simulations were done of a number of different sizes of v-groove waveguides in order to form an understanding of the effect of waveguide size on the propagation loss. Fig. 2.9 shows the results of these simulations. Each data point represents the average loss of TE and TM at a distance of 1 cm along the waveguide. A distance of 1 cm was chosen as it corresponds to the distance between the edge of the chip and the end-facet for the fabricated devices.

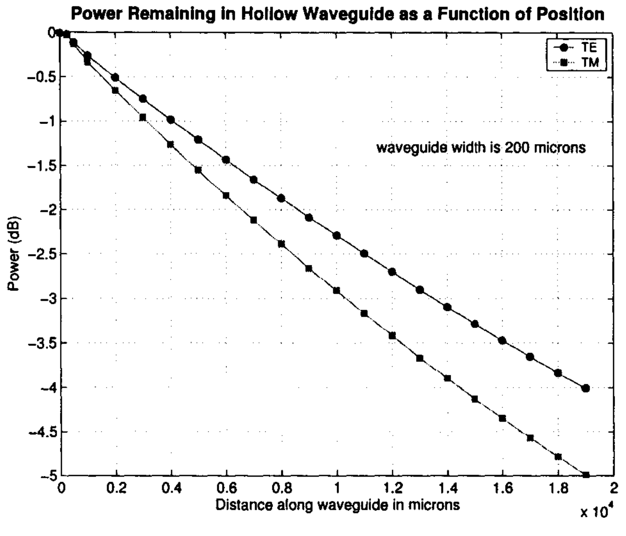

Figure 2.8: Power as a function of distance along a 200 μm wide hollow v-groove waveguide

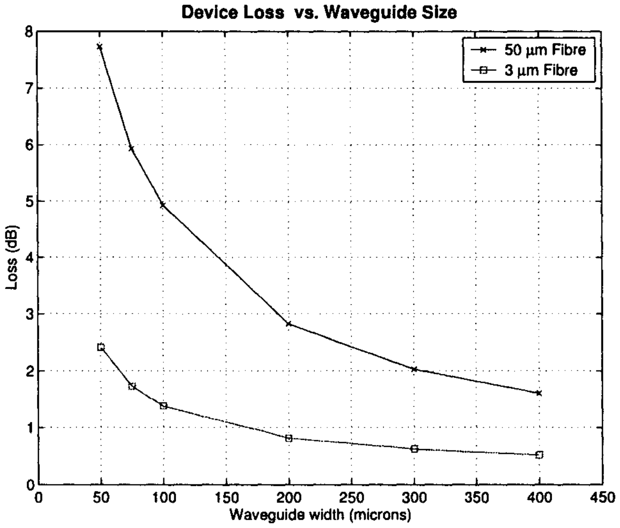

Figure 2.9: Variation of loss predicted by simulation in hollow v-groove waveguides as a function of waveguide size

Two simulation runs were done corresponding to the two different types of optical fibre that were used to test the waveguides. The first simulation run was done using a ray input file that corresponded to the characteristics of a 50 μm diameter core multimode fibre. The rays were launched from within a 50 μm diameter circle with an angular divergence of 12°. This corresponds to the 0.22 numerical aperture (NA) specification of the fibre. The second simulation run was done to sim-

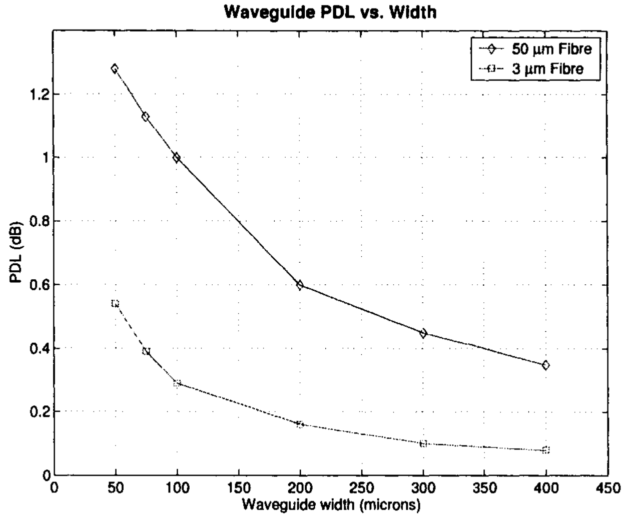

Figure 2.10: Predicted PDL vs. waveguide width at a distance of 1 cm along the waveguide

ulate a singlemode 3 μm diameter core fibre as the input. In this case all rays were launched from within a 3 μm diameter circle with an angular divergence of 5°. This corresponds to a numerical aperture of 0.087.

The NA of both of these fibres was verified experimentally using a beam profiler. This measurement was accomplished by measuring the 1/e points of the beam profile at known distances. The 50 μm fibre had known specifications for its NA, so this measurement reinforced the information provided by the manufacturer. The 3 μm fibre however had no documentation, so determining its NA was necessary to simulate the performance of the waveguides with this type of fibre as the input. The two types of fibre gave significantly different simulation results as shown by Fig. 2.9. As expected from the discussion in Sec. 2.1.2.2, the simulations of the fibre with higher NA, and therefore higher angular spread of rays, predicted higher losses. This corresponded well with the measured optical performance of the waveguides (more details to follow in Sec 4.1).

As can be seen from Fig. 2.8, the model also predicts more attenuation for the TM polarization mode than for the TE mode. By taking the difference between the power in the TE and TM modes, the polarization dependent loss (PDL) can be predicted. The PDL vs. waveguide size is given in Fig. 2.10. As with the loss, the measured PDL of the waveguide is also dependent on the input conditions. This is due to the input rays with greater divergence angles contributing more to the PDL. Fig. 2.11 shows the reflectance coefficient for an air/gold interface for varying angles of incidence. For this interface, the largest difference in reflectance between the two orthogonal polarization states is at about 75° to the normal. This angle is referred to as the principal angle.

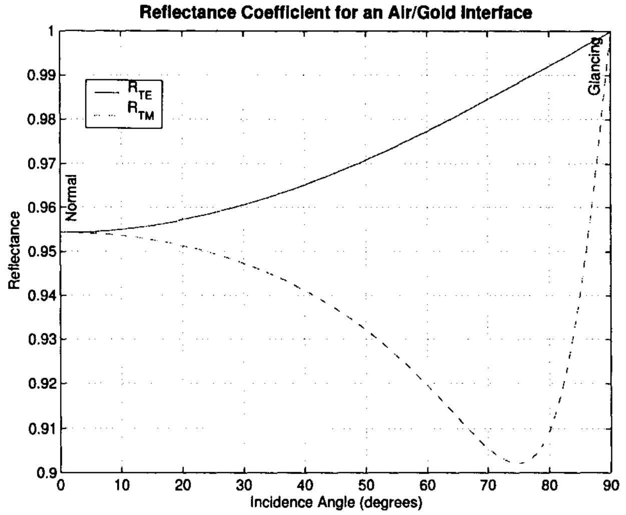

Figure 2.11: Reflectance of an air/gold interface

Both the 50 μm fibre and the 3 μm fibre don't have a divergence that high, but the closer the incidence angle of a ray is to the principal angle the more polarization dependence it sees. Since the 50 μm fibre has more rays closer to the principal angle it is expected that it will show more polarization dependence.

The PDL of the fabricated waveguides was measured and the results are in Sec. 4.1.

2.2.1.3 Side and Top View

A side and top view of the simulation can also be constructed as a visual aid that indicates how power flows through the waveguide. These views are built by projecting the ray onto the appropriate plane (side or top) and then lighting up all the pixels in between reflection points. The algorithm that calculates the pixels to light up is the Bresenham line algorithm which is well known in computer science [50].

Refraction at the waveguide defining planes can also be allowed. If the index of refraction at a plane is purely real (no imaginary component), refraction can be enabled as an option passed into the simulation code. This allows hollow waveguides with glass walls to be modeled. In the work presented here, the v-groove waveguides have a glass window placed above the end facet. Fig. 2.12 was created by taking the output from a simulation of a 400 μm wide hollow v-groove waveguide and using it as the input to a different waveguide structure that had glass as the upper plane instead of gold. The other three planes, the v-groove side walls and the end facet still have the index of refraction of gold. Refraction at the lower glass interface can be clearly seen.

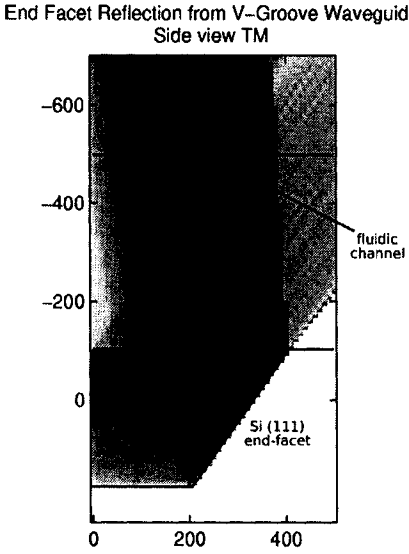

Figure 2.12: Sideview of simulation output showing reflection off an end-facet and refraction at the air-glass interface

2.2.1.4 Output Plane

As well as being used as the input to a subsequent simulation, the output plane can provide useful information for designing the devices detailed in this work. When using the hollow v-grooves and end facet as a means to deliver light to the fluidic channel, it is important to know what the excitation profile looks like. Fig. 2.13 shows the output of a 400 μm wide waveguide after reflection from the end facet 500 μm above the waveguide. From this output, the beam location and dimensions at the location of the fluidic channel can be determined. It is interesting to note that the scatter pattern predicted by the simulations was observed when testing the waveguides.

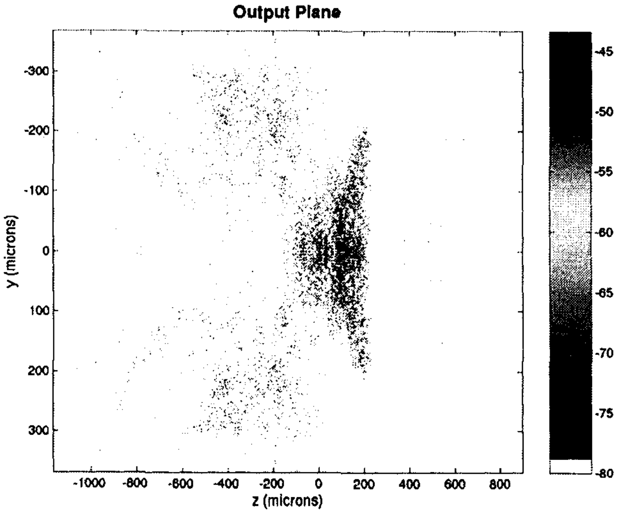

Figure 2.13: Output plane located 500 μm above the end-facet shown in Fig. 2.12

Chapter 3

Design and Fabrication

3.1 Design Overview

The design of the chips took into account different potential uses, as illustrated in Fig. 3.1. The cross chip design was intended for use in capillary electrophoresis analyses. The intersection can be used to create a plug that can be forced down the longer separation channel with a high electric field. Collection waveguides along the separation channel can be used as the detection points. The PCR chip was designed with real time polymerase chain reaction (RT-PCR) in mind. It has two ports with a 10 μL microreactor at the centre. Large collection waveguides underneath the PCR reservoir are a means of guiding emitted fluorescence to the edge of the chip. The 'T' chip and the 'H' chip are potentially useful for applications involving sorting and separating particles or cells. The 'H' chip could be used to mix particles at one intersection and then separate them at the other. This would be useful for testing particle sorting instrumentation.

The waveguides were envisioned to be either a means of exciting fluorescence in the biochip, or a collector of emitted fluorescence. Waveguides used for excitation were designed to be smaller (50, 75 μm) so that the excitation would be more spatially localized. Waveguides designed for fluorescence detection are larger (200, 300, 400 μm) to increase the collection area of the end facet.

Since the silicon crystal geometry defines the (111) planes, the end facet of the hollow v-groove waveguide is formed at 54.74° ($\arctan\sqrt{2}$) to the surface of the wafer. Ideally, an angle of 45° would be more convenient for the application of coupling light from the waveguide upward through a fluidic layer. The deviation from 45° causes a ray travelling down the waveguide parallel to the (100) plane to be reflected upward off the (111) end facet at an angle of 19.5° to the wafer surface. This is an important detail when considering the placement of the fluidic channels with respect to the waveguide end facet. More details on the design geometry of the end facet to microfluidic channel

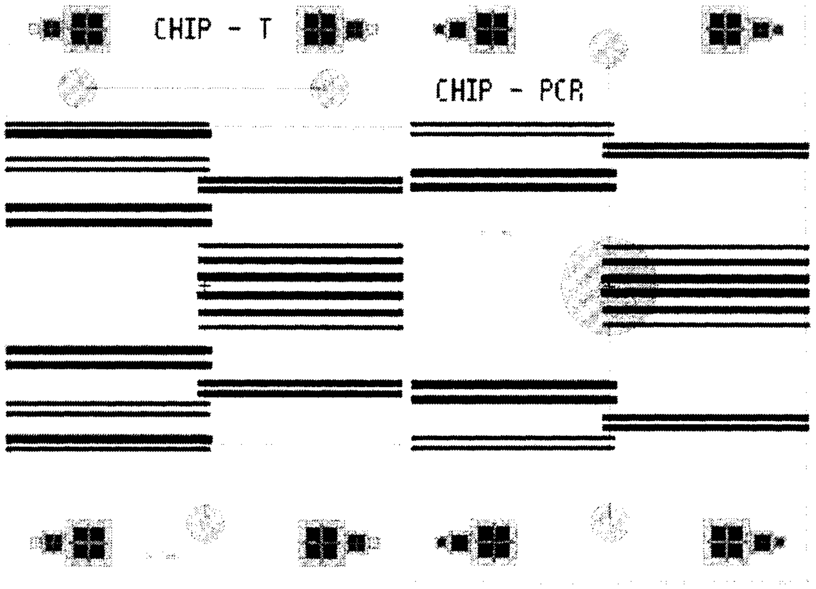

(a) T-chip design - potentialy used for mixing or cell sorting and switching applications

(b) PCR design - intended for PCR analyses or possilby real-time PCR

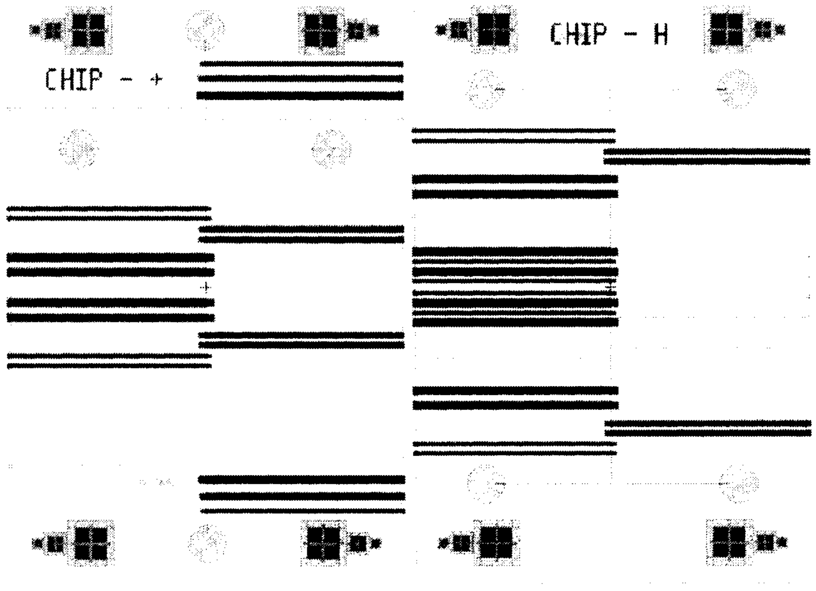

(c) Cross chip design - meant for capillary electrophoresis

(d) H-chip design - for mixing and / or swtiching applications like cell sorting

Figure 3.1: Chip designs

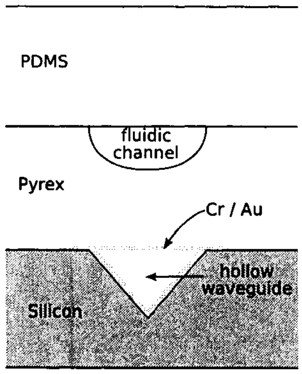

Figure 3.2: Device crossection. Three material layers make up the two functional layers of the device, fluidics and optics.

distance are given in Appendix C.

3.2 Fabrication Overview

The two functional layers of the fabricated device, fluidics and optics, are made of three material layers, PDMS, Pyrex 7740 glass and silicon as shown in Fig. 3.2.

The PDMS layer functions as a cap for the microfluidic channels. The pyrex component has etched fluidic channels on one side, and metalized stripes on the other which serve as caps for the v-groove waveguides. The hollow waveguides are v-groove trenches machined into the silicon layer of the device.

A working knowledge of the theory behind the important processing steps increases the chances for success in fabricating devices. To this end, the basic theory of the important process steps will be presented here. A detailed step-by-step guide to the entire fabrication process is included in Appendix B, which will be referred to as necessary.

A general overview of the fabrication process is shown in Fig. 3.3. A total of three masks were needed to build the device. One mask was used for patterning the KOH etch features (mask #1), one for the fluidics (mask #3), and one for the Cr/Au on the reverse side of the pyrex (mask #2). Mask #2 was also used for patterning the Cr/Au that was sputtered into the v-grooves. Considering that the metal on the reverse side of the pyrex does not cover the end facets, mask #2 had to be modified when being used to pattern the Cr/Au in the v-grooves. The modification was a small narrow strip of tape which was placed in the middle of each die over the end facets (on the top side of the mask). This shields the resist over the end facets during exposure so metal that was covering the end facets

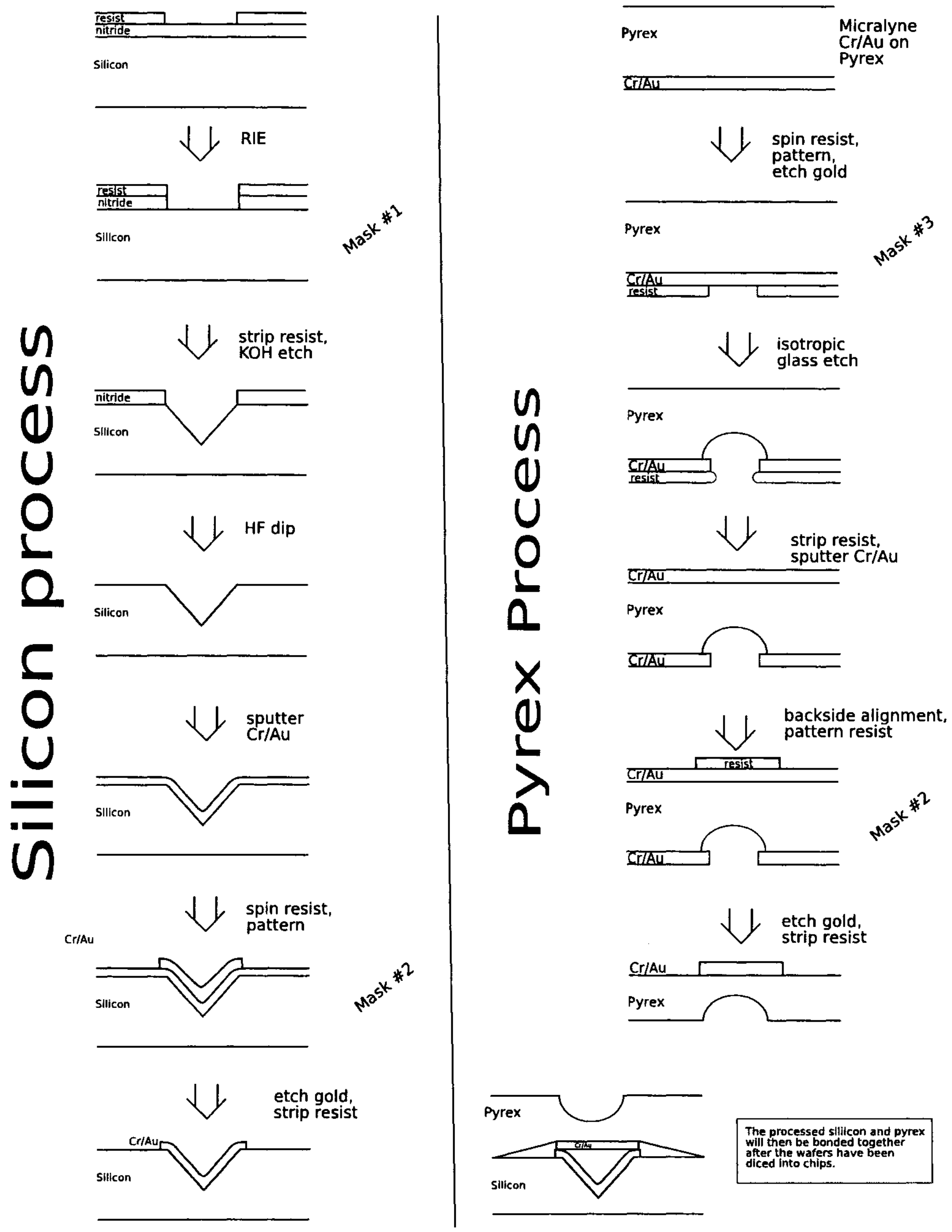

Figure 3.3: Fabrication process flow

remained after the subsequent Cr/Au etch.

The masks are described further in Appendix D.

3.3 Anisotropic Silicon Etching

Etching can be divided into two categories, isotropic and anisotropic. Isotropic etching is direction independent, that is, etching occurs at the same rate in every direction. This produces features that have a round geometry. See Fig. 3.4 (taken from [51]).

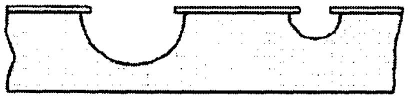

Figure 3.4: Isotropic etching

Anisotropic etching is direction sensitive. Wet chemical anisotropic etching is well known and has been in use since the '60s [52]. This is the simplest way to "machine" structures in silicon with well known geometry.

An anisotropic etchant preferentially etches some crystal planes faster than others. As shown in Fig. 3.5, the crystal structure of silicon has a very high packing density in the (111) plane. During chemical anisotropic etching, the silicon (111) planes etch much slower than any of the other crystal planes. Sato et al. [53] tabulated the etch rates of different silicon crystal planes in typical anisotropic etch conditions (70^oC, 30% w/w KOH), see Table 3.1. The etch rate of the different planes is given in μm/min for different concentrations of KOH, and the anisotropy relative to the (111) plane (Rxxx/R111) is indicated in the brackets. The plane with the second slowest etch rate is indicated by an asterisk. It can be seen that the (111) planes etch two orders of magnitude slower than any other crystal plane. This leaves the (111) planes to be the defining features after the etch. Using the knowledge of the relative crystal plane etch rates and careful mask design, interesting and useful structures can be machined in silicon.

Depending on the desired features, the direction of the (111) planes relative to the wafer surface is important. The two silicon wafer types most often used for anisotropic silicon etching are those that have surface orientation of (100) and (110). Wafers with (100) surface orientation etch inverted pyramid type structures due to the orientation of the (111) planes as illustrated in Fig. 3.6. The (111) planes are at an angle 54.74° to the surface of a (100) silicon wafer. Wafers with (110) orientation

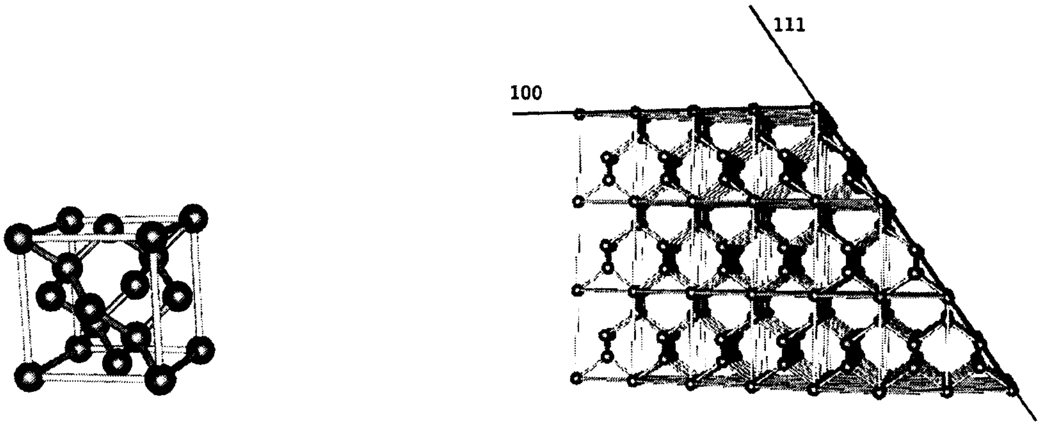

(a) silicon unit cell

(b) silicon crystal with cleave along 111 plane

Figure 3.5: Silicon crystal structure

Crystallographic orientation	30%	40%	50%
(100)	0.797 (159)	0.599 (67)	0.539 (60)
(110)	1.455 (291)	1.294 (144)	0.870 (97)
(210)	1.561 (312)	1.233 (137)	0.959 (107)
(211)	1.319 (264)	0.950 (106)	0.621 (69)
(221)	0.714 (143)*	0.544 (60)*	0.322 (36)*
(310)	1.456 (291)	1.088 (121)	0.757 (84)
(311)	1.436 (287)	1.067 (119)	0.746 (83)
(320)	1.543 (309)	1.287 (143)	1.013 (113)
(331)	1.160 (232)	0.800 (89)	0.489 (54)
(530)	1.556 (311)	1.280 (142)	1.033 (115)
(540)	1.512 (302)	1.287 (143)	0.914 (102)
(111)	0.005	0.009	0.009

Table 3.1: Silicon crystal plane etch rates in 30% (w/w) KOH, at 70^oC

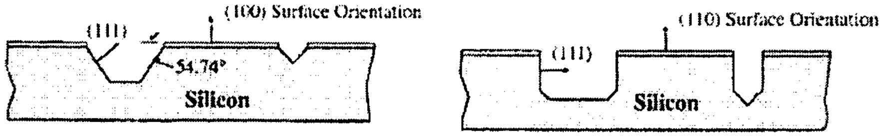

(a) (100) Si wafer

(b) (110) Si wafer

Figure 3.6: Anisotropic etching

can be etched to form structures with vertical walls since the important (111) planes are orthogonal to the wafer surface [52, 54] (see Fig. 3.6 for illustration). It should be noted that it is possible to etch silicon with 45° planes, but it is difficult and the resulting planes do not have good surface quality [39].

The three most popular anisotropic etchants of silicon are potassium hydroxide (KOH), ethylenediamine pyrocatechol with water (EDP or EDW) and tetramethyl-ammonium hydroxide (TMAH). When choosing an etchant the primary factors to be considered are: silicon etch rate, masking material (and required mask thickness), etch smoothness, toxicity, and availability. A comparison of the most popular anisotropic etchants is given in Table 3.2 (adapted from [51]).

KOH was the etchant used for this work as it is readily available and relatively safe to use. EDP is reported to be the best etchant in terms of surface quality achieved on the silicon (111) planes and the reliability of the etch reaction [55]. The main drawback with EDP is that it is a dangerous and highly toxic substance that requires great care in processing. EDP was ruled out for this work due to the dangerous nature of the substance and by the fact that the University of Alberta NanoFab does not currently allow EDP into the fabrication facility. To use EDP for this work would have required securing another venue for the anisotropic etch step.

	KOH	EDP	TMAH
Availability	common	moderate	moderate
Si Etch Rate (μm/min)	1 to 2	0.02 to 1	~1
Si roughness	low	low	variable
Nitride etch rate	low	low	1 to 10 nm/min
Oxide etch rate (nm/min)	1 to 10	1 to 80	~1
Safety	moderate	low	high

Table 3.2: Comparison of common anisotropic etchants for silicon

feature width (μm)	depth of v-groove (μm)
50	35
75	53
200	141
300	212
400	283

Table 3.3: Nominal depth of v-groove for designed feature widths

In order to achieve smooth (111) planes, the anisotropy with respect to the (111) planes should be as high as possible. Using a KOH solution with no additives (some people like to put IPA in the solution), the highest anisotropy is achieved at a KOH concentration of about 30% (w/w). Results of Price [56] and Herr [57] suggested that a KOH concentration of around 30% achieved the highest anisotropy with respect to the (111) plane. Discussion with individuals that have done significant work with KOH as an anisotropic etchant also suggested 30% as optimal [55, 58].

For this work, a KOH concentration of 30% (w/w) at a temperature of about 80^oC was used. No IPA or other surfactant was added to the solution during etching.

It is possible to put all different sizes of features on one mask due to the nature of the anisotropic etch. Once the (111) planes meet in a 'v', there are no more exposed planes with high etch rates available. Therefore, 50 μm wide features will effectively stop when the (111) planes meet at a depth of about 35 μm (see Table 3.3 for a list of feature width and corresponding v-groove depth).

The choice of material for the masking layer of the KOH etch step turned out to be the most critical for the fabrication aspect of this project. To achieve features of significant depth (greater than 280 μm), the selectivity of the etchant to attack the silicon and not the etch mask is an important consideration. A secondary consideration was how easily the masking layer could be removed after the anisotropic etch. For this work, both silicon oxide and silicon nitride were investigated as materials for the KOH etch mask.

Initially, thermal silicon oxide was chosen as the etch mask due to the ease with which it can be removed after the etching step and its immediate availability. Given that the reported etch rate of thermal oxide in KOH is on the order of 1-10 nm/min [51], the oxide would need to be quite thick to etch the silicon to a depth of 283 μm (corresponds to a 400 μm wide mask opening etching to completion). The oxide etch rate was later measured to be about 13 nm/min with a KOH temperature of 89 ^{o}C. The silicon etch rate was measured to be 1.8 μm/min, so the total time to etch 283 μm was about 157 minutes. The oxide thickness then needed to be 2.04 μm. A thermal oxide with thickness of over 2.2 μm was achieved by oxidizing a wafer in the minibrute furnace for a total of about 22 hours (oven was turned off overnight, then switched back on in the morning).

Thermal oxide turned out to be a poor choice for the masking layer material as it consistently gave unacceptable results for anisotropic etching. The walls were very jagged and would obviously not work for hollow waveguides. The source of the problem was initially thought to be contamination of the etch bath, possibly the reflux column. To this end the reflux column was not used for subsequent etches. The poor results continued, so the container used to do the etch was replaced with a new one that was only used for KOH etching of this work. This way contamination was controlled, as all chemicals that touched the inside of the container were known.

After much investigation, the source of the problem was revealed to be bad lithography of the oxide mask. During the opening of the oxide mask with a BOE etch, the HPR504 resist started to lift away from the oxide. Normally this is not a problem, as the BOE step for a normal oxide mask (1 micron thickness) is on the order of 30 minutes, not 90 minutes as was the case with the 2 micron thick mask. This problem was not obvious at first. The interface line between the oxide and the silicon was straight, but the top edge of the oxide was not. This was due to the resist lifting part way through the BOE step. This upper edge is what defines the KOH etch mask as the etch progresses.

In the end, using silicon nitride as the mask layer proved successful. Nitride is not appreciably etched in KOH [52] and therefore makes a good hard etch mask. The best type of nitride for use as a KOH etch mask is a low stress nitride. For this work, low pressure chemical vapour deposition (LPCVD) silicon nitride wafers manufactured by Strata Glass [59] were purchased from Norcada. Using a low stress nitride reduces the lifting and cracking that can occur if a high stress layer is used as a mask. The silicon nitride was removed after the anisotropic etch by a 90 minute dip in 49% HF.

LPCVD nitride is also a better material for the KOH etch mask due to the fact that it can be deposited without subjecting the silicon wafer to high temperature. During high temperature processing steps like thermal oxidation, oxygen in the wafer will form precipitates. These precipitates form defect sites that will be evidenced as surface roughness after the KOH etch [54].

3.3.1 Accurate Alignment to Crystal Planes

An important consideration when fabricating anisotropically etched features is the alignment of the mask to the silicon crystal plane. If the mask feature is misaligned with respect to the silicon crystal plane, dislocations will be seen along the sidewalls. These sidewall dislocations will cause extra loss for hollow waveguide applications. Silicon wafers have a machined flat that is aligned to the (110) plane of the crystal. However, the wafer flat tolerance is typically accurate to only +/-0.5 degrees.

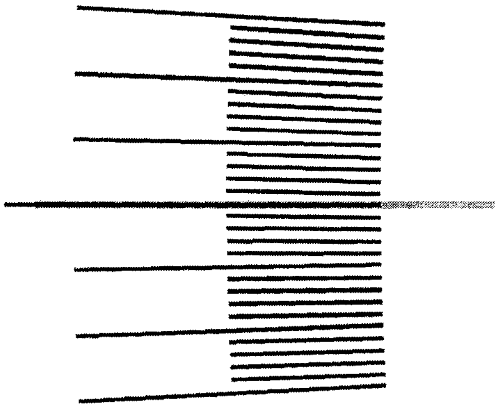

Figure 3.7: KOH pre-etch feature

Also, a slight radius to the flat can cause additional error when aligning the mask to the wafer flat. To mitigate this problem, a pre-etch step is needed to accurately determine the exact crystal plane of the wafers. To this end, a pre-etch feature was placed on the KOH etch mask near the edges. The pre-etch feature, shown in Fig. 3.7 consisted of a partial wagon wheel like pattern with spokes every 0.2 degrees. The longer spokes were placed every 1 degree. The design for the pre-etch feature was influenced heavily by [52] and [60]. The rest of the mask was blocked by tape during exposure of the pre-etch features so that only the pre-etch features were exposed.

When this feature was etched anisotropically and inspected under a microscope the crystal planes of the wafer can be determined within +/-0.1 degrees. Therefore, the alignment accuracy was improved by a factor of 5. The dislocations due to misalignment with the crystal can be seen in the etched features shown in Fig. 3.8.

For a more detailed description of the KOH pre-etch step see Appendix B.1.

3.4 Metal Layer Deposition and Characterization

This section describes the considerations for the metal layer as well as the deposition details and method of characterization.

To increase the reflection coefficient of the hollow waveguides, it was necessary to coat them with a metal. Metals that were considered included chrome, gold, platinum, titanium, silver, copper, and aluminum. To evaluate the suitability of a metal for the hollow waveguide coating, a few factors were considered. The reflectance of the material should be as high as possible and should not deteriorate with time (by oxidization). Another consideration was the availability of etchants

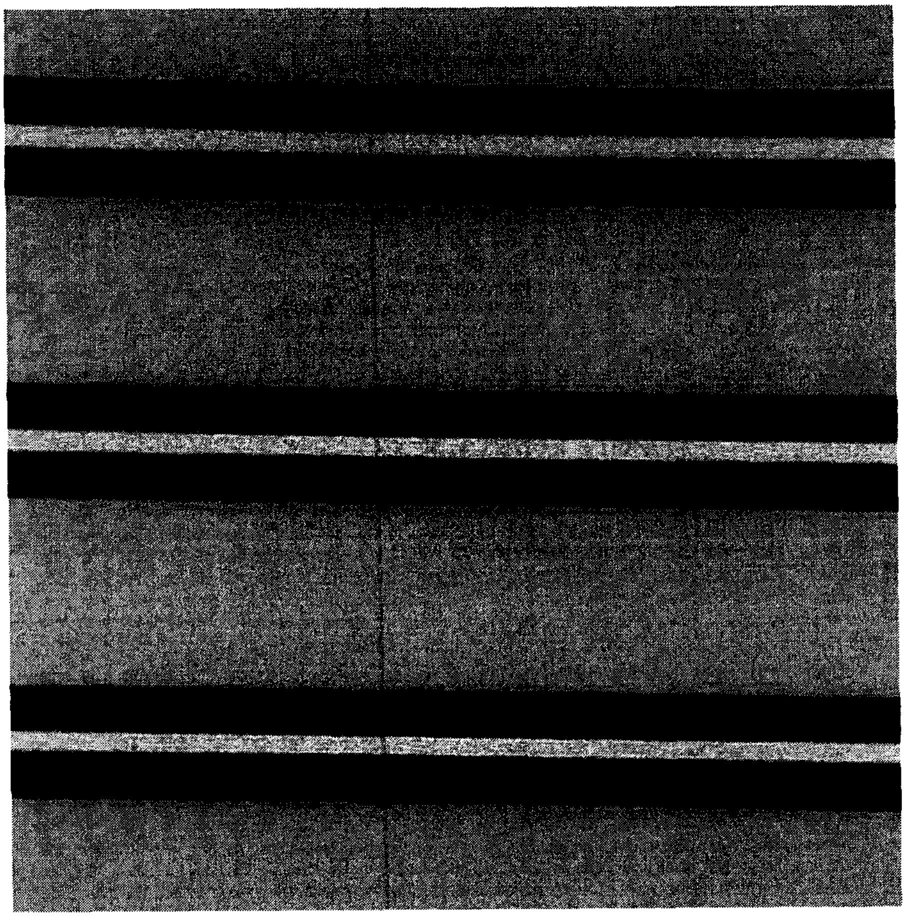

Figure 3.8: Pre-etch features showing dislocations due to misalignment

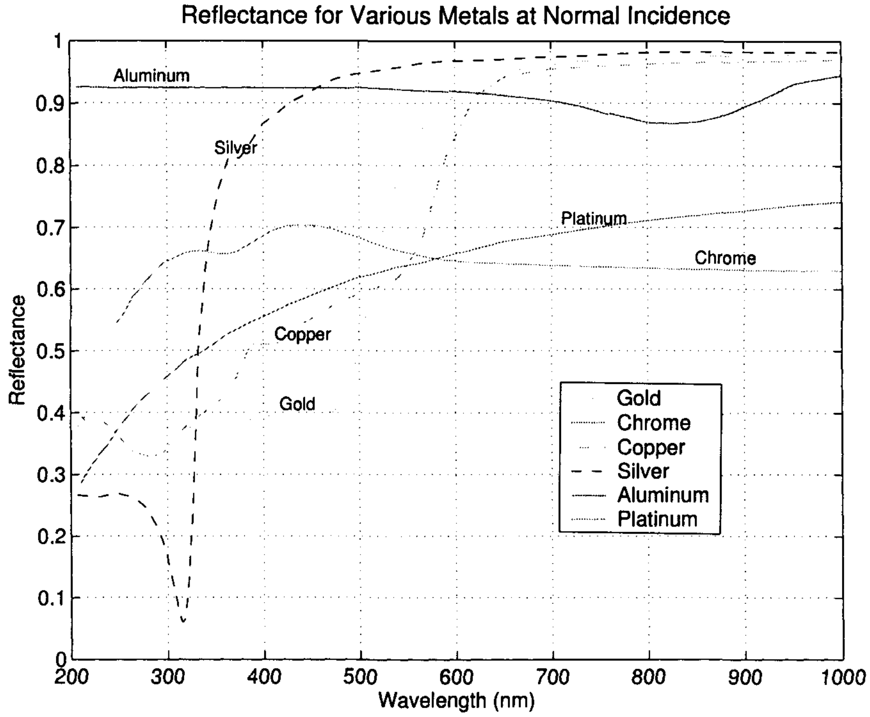

Figure 3.9: Reflectance of various metals considered for the reflective coating of the hollow waveguides

for patterning the metal after sputtering onto the substrate. Unlike most thin film applications, stress in the film was not a concern since it is only needed as a reflective surface. Fig. 3.9 shows the reflectance of the metals that were considered. These curves were generated by calculating the reflectance based on their real and imaginary index of refraction values (n and k). These values were extracted from the variable angle spectroscopic ellipsometer (VASE) as material constant files. The original tabulated values can be found in Palik [61].

Chrome and platinum are quickly ruled out due to their poor reflectance when compared to the other metals shown. Of the remaining metals, reflectance degradation due to oxidation will affect copper, aluminum and silver. This left gold as the best choice. If degradation of the reflectance due to oxidation were not an issue, silver would obviously be the best choice as it has excellent reflectance over the entire visible spectrum (400-700 nm). It is important to note that gold will not work very well if the waveguides are to be used for any wavelengths shorter than about 600 nm. The fluorescence experiments in this work were performed with 635 nm lasers and dyes that fluoresce in the longer wavelengths.

A metal film of Cr/Au was sputtered onto the substrates as the reflective layer for the hollow waveguides. The chrome is needed as an adhesion layer for the gold. The thicknesses of the chrome and gold layers was 30 nm and 75 nm respectively. The metal layer needed to be as thin as possible to ease concerns of bonding. On the other hand, the gold layer had to be thick enough to completely reflect light. To determine the minimum thickness of the metal layer needed, it is useful to calculate the skin depth of the metal. The skin depth is the distance into the metal at which the electric field decays to $1/e$ of the incident value. If the imaginary part of the material index of refraction is known the skin depth can be easily calculated according to the following formula.

$$\delta_s = \frac{\lambda_o}{4\pi k} \tag{3.1}$$

where δ_s is the skin depth, λ_o is the wavelength of light in a vacuum and k is the complex part of the index of refraction. For gold at a wavelength of 670 nm, k is approximately 4 (see Fig. 3.10). This corresponds to a skin depth of 13 nm. To ensure that light would not penetrate through the gold, the sputtered film thickness was chosen to be much greater than the calculated skin depth.

3.4.1 Measurement of the Metal Film Properties

The complex index of refraction of the sputtered Cr/Au film was measured with a variable angle spectroscopic ellipsometer (VASE). Results matched tabulated values for Au very well [61] as shown in Fig. 3.10. These results were used in the simulation model (see Sec. 2.2) in an attempt to match simulation with measured waveguide losses (see Sec. 4.1).

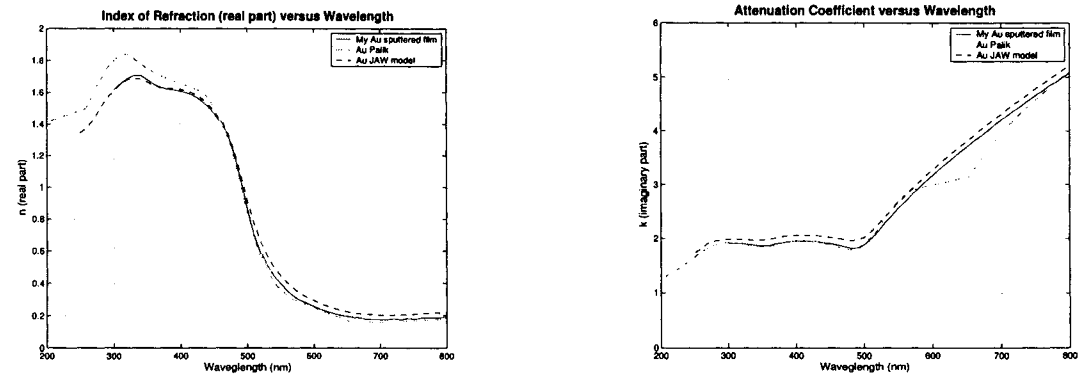

(a) real part of the index of refraction

(b) imaginary part of the index of refraction

Figure 3.10: Gold index of refraction

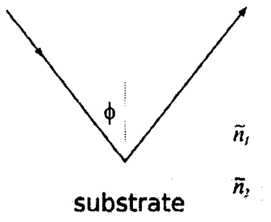

Figure 3.11: Reflection from a substrate

The VASE is able to measure the complex index of refraction or thickness of a material by analyzing light that is reflected from the sample. The ellipsometer analyses the reduction in amplitude as well as the phase shift between two orthogonal polarization states after reflection from the material surface. Using these two pieces of information, quantities such as film thickness and index of refraction can be determined by numerical fitting with a material model.

The fundamental equation of ellipsometry is given in Eq. 3.2. The quantities that are measured by the ellipsometer are ψ and Δ which contain information about the ratio of the complex reflection coefficients of the material.

$$\rho = \frac{R^p}{R^s} = \tan \Psi e^{i\Delta} \tag{3.2}$$

In the case of a substrate, the values of Ψ and Δ can be easily related to n and k through Eq. 3.3. A material can be considered a substrate if the reflected light is only due to the initial surface, not a combination of reflections from multiple interfaces beneath the initial surface. For the Cr/Au sample measured in this work, the Au was thick enough to be considered a substrate, so the measurement was fairly straight forward. In the case of a more complicated thin film sample, the reader is referred to a more thorough explanation of spectroscopic ellipsometry [47].

$$\tilde{n}_2 = \tilde{n}_1 \tan \Psi \sqrt{1 - \frac{4\rho \sin^2 \phi}{(\rho + 1)^2}} \tag{3.3}$$

3.5 Wet Etching

3.5.1 Cr / Au Etch

Gold and chrome etching are both standard NanoFab processes. The gold is etched with Au etchant, which is a mixture of hydroiodide acid (HI) and potassium iodide (KI). The chrome etchant is ceric ammonium nitrate, nitric acid and water. Gold and chrome etching is needed three times in the fabrication process, to open the Cr/Au mask for the glass etch, and to pattern both the silicon and the pyrex pieces after the sputter step.

3.5.2 Glass Etch

The top side of the wafer was etched with borofloat etch ($HF/HNO_3/H_20$ 20:14:66) to form the fluidic channels using a layer of Cr/Au as the hard mask layer.

Etching of microfluidic channels in glass is highly dependent on the quality of the masking layer, Cr/Au in this case. If the metal film has a lot of stress in it, the etched features will be much wider than expected. This is due to the stressed metal lifting away as the etch proceeds, causing a high undercut rate. To achieve the expected feature sizes, a low stress Cr/Au film is imperative. To this end, pyrex wafers with a low stress Cr/Au film already deposited where obtained from Micralyne as an in-kind contribution to the project.

3.6 Dicing and Bonding

Dicing of the pyrex and silicon components was done on the diamond touch saw and disco saw respectively. The diamond touch saw is only used for glass substrates and the disco saw is meant for silicon substrates. The two saws have different kerf widths (width of material removed after a cut). The diamond touch kerf is about 250 μm, while the disco saw kerf is only 50 μm. The different saw kerfs made cutting the chips to the same size a little more challenging but accomplishable. To further complicate things, 1 mm from each side of every chip was cut off to fix a mistake in the KOH mask layout (mask #1). The mistake was due to the dicing marks and the waveguide features meeting in a convex corner that was substantially undercut during the KOH etch step. Further detail is available in Appendix B.3.

After dicing the wafers into chips, the matching chips from the pyrex and silicon wafers were fastened together. It was not possible to bond the wafers and then dice them due to the nature of the hollow waveguides. The dicing saws use water jets to clear debris from the blade during the dicing procedure. The water would inevitably carry debris into the hollow waveguides compromising their performance. Since the hollow waveguides are only open on one end, cleaning them would be impractical.

3.6.1 Bonding Pyrex to Silicon

Fastening the silicon and pyrex components together turned out to be a bigger challenge than initially foreseen. The original intention was to contact bond them, then strengthen the bond by anodically bonding them together. The contact bond was not anticipated to be of great quality due to the metal features left between the components (refer to Fig. 3.3 for clarification). It was just meant to initiate contact so that the chips could be aligned in the clean room and then brought out for anodic bonding.

Contact bonding is done by bringing two flat, clean surfaces together such that they are held together by the Van der Waals forces [62]. There are three different types of Van der Waals forces: orientation force, induction force and dispersion force. The orientation force is caused by the dipole-dipole attraction of two polar molecules. The induction force is generated when a polar molecule induces a charge separation (weak dipole) in a non-polar molecule and attraction occurs. The dispersion force is caused by an induced-dipole-induced-dipole interaction between two molecules. This is possible because at any moment in time there exists a small dipole on one of the molecules due to a non-uniform distribution of electrons. This dipole then induces a dipole in the other molecule and the interaction begins.

The range of the Van der Waals force between two molecules is very short ($F \propto r^{-7}$) [62]. However, when considering macroscopic body interactions, such as two parallel plates, the effective force is made up of contributions from all the surface molecules. The van der Waals force per unit area between two flat plates decreases with the inverse third power of the separation distance.

$$F_v = \frac{A}{6\pi d^3} \tag{3.4}$$

where A is the Hamaker constant and d is the separation between the two plates. For silica-air-silica the Hamaker constant is $6.5 * 10^{-20} J$ [62, p. 18-19]. If during bonding there is a particle or defect in the surface that leaves circular regions of unbonded area, the radius of the unbonded region can be calculated (for (100) Si) as $R = \left[0.73 E t_w^3/\gamma\right]^{1/4} h^{1/2}$ where E is the Young's modulus, t_w is the wafer thickness, γ is the surface energy of the wafer, and h is the radius of the trapped particle (see Fig. 3.12 for clarification). The radius of an unbonded area for a silicon wafer of thickness 525 μm, and surface energy of 100 mJ/m^2 is shown in Fig. 3.12 (taken from [62]). Using this analysis and Fig. 3.13 (taken from [62]), the voids in the contact bond due to the metal features between the pyrex and silicon were anticipated to be about 1.5-2 mm.

To further increase the probability of a successful contact bond, the silicon and pyrex surfaces were

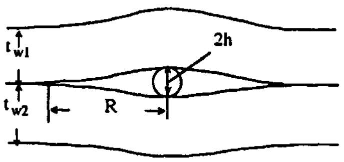

Figure 3.12: Trapped particle in a contact bond

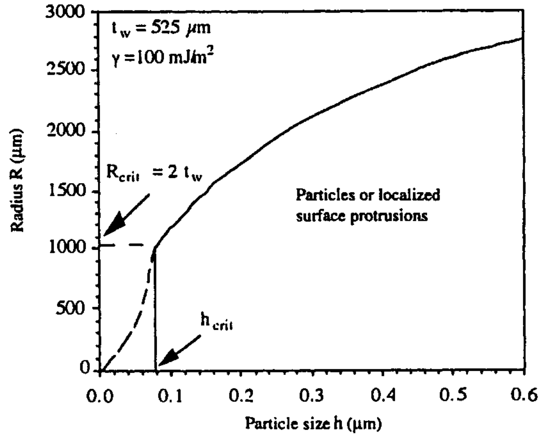

Figure 3.13: Unbounded radius around a particle trapped in a contact bond

treated to increase their hydrophilicity. When two surfaces to be bonded are hydrophilic, the surface flatness requirement for a contact can be reduced due to water molecules bridging the gap between the materials. Various surface treatment methods and a more complete description of the surface chemistry involved can be found in Tong and Gosele [62, pg 57-62]. Surface hydrophilization of the silicon and pyrex chips was accomplished by submerging them in KOH and gently massaging them with a sponge for ~2 minutes (at room temperature, no appreciable etching of the silicon occurred). KOH was chosen as the surface treatment due to its availability and ease of use.

Immediately following the surface treatment, contact bonding of the chips was attempted by mounting the chips to carrier substrates and bringing them into intimate contact. The silicon chip was mounted on a silicon carrier and pyrex chip on a blank mask plate. The alignment and contact was done with the AB-M mask aligner. Despite best efforts, a contact bond was not achieved.

Since the contact bond was unsuccessful, alignment necessary for the anodic bonding process was done manually on a hot plate with the aid of microscope, tweezers and patience.

The first attempt at anodic bonding was done at a temperature of 400 ^oC and with 1000 volts applied across the interface. The bond was initiated with a point probe as the anode, until the bond held when the potential was removed. The point probe was then replaced with a rectangular aluminum anode just slightly smaller than the chip. This was done in order to speed up the bonding process. The total time for the anodic bond was about 1 hour. After the bond was complete, the Cr/Au film looked distorted. The Cr/Au had brown patches believed to be caused by the interdiffusion of the two metals. When this device was later tested, the distortion of the Cr/Au was found to significantly affect the performance of the waveguides (more details in Chapter 4).

A second attempt at an anodic bond was done at 330 ^oC with 1000 volts applied across the pyrex-silicon interface. The lower temperature was used in the hope that the Cr/Au diffusion could be minimized. The total time for the bonding took about 100 minutes. After the bond was complete, the Cr/Au still had significant evidence of diffusion, though slightly less than the initial attempt.

It should be noted that the two pieces were very resistant to bonding. In fact, within a few days, one of the anodic bonds failed and a device fell apart. The reason for the bad adhesion even after anodic bonding is thought to be the large amount of metal left on the silicon chip.

Since anodic bonding was unsuccessful, epoxy bonding was investigated as an alternative means of fastening the chips together. The epoxy bond was performed using the AB-M mask aligner and secured with a UV curable epoxy, Norland optical adhesive (NOA) #61 [63]. This worked relatively well, although the bond was not as intimate as the bond achieved by anodic bonding. When the bond was particularly bad, light leaking from one waveguide to the adjacent one was visible when inspecting the reflections from the end facets under a microscope. Another challenge with the epoxy bond method was keeping the epoxy out of the v-grooves. This required dispensing the epoxy only in the corners of the chips and in very limited amounts.

3.6.2 Bonding PDMS to Pyrex

In recent years, polydimethylsiloxane (PDMS) has emerged as an important material for microfluidic applications. It is optically transparent in the visible region of the spectrum, cures at low temperatures, is biocompatible [29] and can seal reversibly or irreversibly to itself and other materials [28].

PDMS was chosen as the superstrate for the devices fabricated in this work due to its ability to form a reversible bond with glass. The ability to tear off the PDMS after an experiment has been preformed is an advantage when considering the cleaning and reuse of the devices. After removing the PDMS there is no residual left on the surface of the pyrex. The biggest drawback of the PDMS / pyrex bond being reversible is that it cannot stand high pressure flow in the microfluidic channel.

According to McDonald et al. [28] pressures greater than approximately 5 psi in the microchannels will cause the bond to fail.

The 2 mm thick PDMS layer was prepared by casting 10 grams of uncured PDMS and curing agent (10:1 ratio by weight) over a clean silicon wafer. A silicon wafer is used because it is a known flat surface with controllable surface chemistry. The wafer should be cleaned in pirahna if necessary and then treated with hexamethyldisilazane (HMDS). This surface treatment is necessary so that the PDMS will peel off the wafer after curing. If the surface treatment is neglected, the PDMS will be permanently bonded to the silicon.

The cured PDMS was cut to the size of the chips, and then access holes were punched in the locations that would fall above the reservoirs. If both the PDMS and pyrex are sufficiently clean and flat, they will bond together by van der Waals forces when brought into contact. See Appendix B.5 for the complete details.

A complete fabricated device is shown in Fig. 3.14. This particular device is a cross design as evidenced by the pattern of the fluidic channels that connect the reservoirs. The waveguides can be seen between the edge of the chip and the microfluidic channel. The waveguides look brown in color due to the fact that the chrome layer is what is visible from above. At the edge of the chip, the openings to some of the larger v-grooves can be seen. The gold region running down the middle of the chip was left there due to the modification of the Cr/Au etch mask that was necessary to leave metal on the end facets.

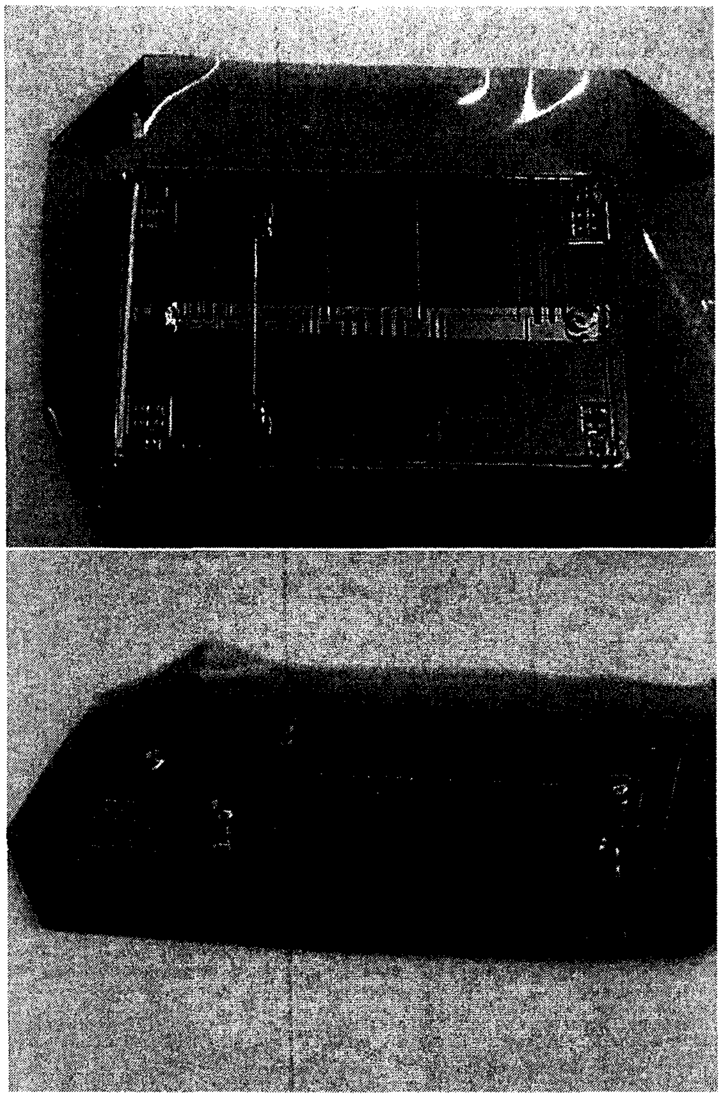

Figure 3.14: Finished device

Chapter 4

Testing and Application

4.1 Hollow Waveguide Performance

The optical performance of the hollow v-groove waveguides was tested using the setup shown schematically in Fig. 4.1.

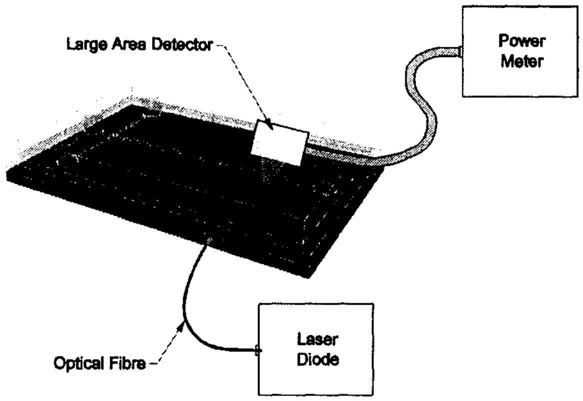

Figure 4.1: Loss measurement setup

Two types of optical fibre were used for the measurements. To measure the loss of the larger waveguides (400, 300, 200 μm widths), a 50 μm core diameter multimode fibre was used to deliver 635 nm light to the edge of the chip. The fibre was aligned to a hollow v-groove waveguide while a large area power meter gathered the light reflected upward from the end facet. The fibre and detector position were both optimized to achieve the best signal. The loss of the waveguide was then determined by taking the difference between the detected signal power and the launched power measured at the fibre end.

Separate measurements were done using a singlemode fibre obtained from TRLabs. The exact specifications of this fibre were unknown, but it was believed to be a 3 μm core diameter which was singlemode at red wavelengths. This fibre was used to deliver 650 nm light to the smaller (50, 75 μm) waveguides. The intent was to be able to test the smaller waveguides without excess coupling loss due to light exiting the fibre missing the core of the hollow waveguide. At the same time, the larger waveguides were measured again using this smaller fibre. The results of all the loss measurements are shown in Fig. 4.2.

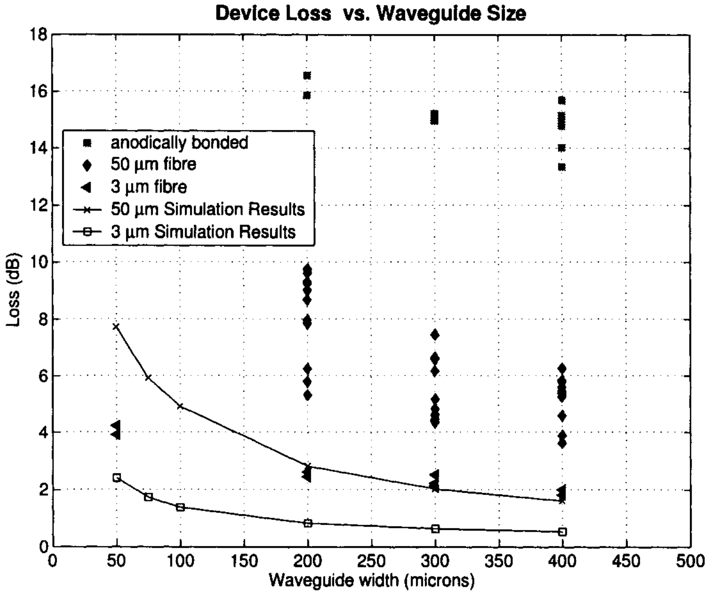

Figure 4.2: Loss measurements

The anodically bonded devices showed significantly higher loss than the epoxy bonded devices. This was due to distortion of the Cr/Au thin film at the elevated temperatures needed for the anodic bonding process. It is suspected that the metals interdiffused causing the film to be a mixture of gold and oxidized chrome. Also interesting to note was that the measurements using the 50 μm multimode fibre showed higher loss than the measurements done with the 3 μm singlemode fibre. These observations agree with the trend predicted by the simulations. See Sec. 2.2.1.2 for a discussion on the effect of the fibre numerical aperture on the predicted loss of the waveguide.

A few extra observations were made about the loss measurements. Waveguides positioned farther away from a fluidic channel exhibited lower losses. Due to a design mistake in the mask set, the end facets of some waveguides were offset from the ideal position and therefore didn't illuminate the fluidic channel optimally. This design flaw, which reduces the efficiency of the coupling to the fluidic channel, can be seen as a benefit when trying to measure the loss in the waveguide. Having the fluidic channel out of the path of the reflected beam meant there was less scattering and hence lower measured loss. Waveguides whose end facets were correctly positioned did measure noticeably higher loss due to refraction and scattering from the fluidic channel. Of course, this doesn't mean that these waveguides are more lossy than others that were positioned incorrectly. Measuring the actual coupling efficiency to the fluidic channel would be useful information to obtain; however there is no immediately apparent method for achieving this.

On waveguides that did not illuminate the fluidic channel well, the repeatability from measurement to measurement was +/-0.1 dB. On devices where the waveguide end facet is properly illuminating the fluidic channel, the repeatability is poor. This is likely due to the amount of refracted and scattered light that is contributing to the measurement.

After considering the effect of the fluidic channels on the waveguide loss measurements, it is apparent that there is still a discrepancy between the simulations and the measurements. Two factors are proposed as possible explanations for this. First, the intimacy of the silicon/pyrex bond affected the loss of the waveguides. Waveguides positioned in regions of a chip that were bonded well (few interference fringes observed) had less loss than those positioned in regions that were bonded more poorly (many interference fringes visible). This would imply that bonded guides were leaking light out of the corners of the v-grooves. Light leaking to the adjacent waveguide was visible under the microscope when the bond was not very good. Second, the simulations assume perfectly planar geometry for the waveguide. This idealization was most likely not the reality of the fabricated devices. Roughness of an anisotropically etched feature is generally on the order of hundreds of nanometers and can have a pyramid-like shape [52]. Simulation of waveguide surfaces with roughness similar to those that are anisotropically etched could reduce the discrepancy between the measurements measurements and simulations. A more useful approach would be to refine the etch chemistry such that the etched features approach the idealized planar surfaces.

Measurements of the waveguide polarization dependent loss (PDL) of the waveguides were also done. The measurement setup is shown schematically in Fig. 4.3. A polarization controller was used to manipulate the polarization of the light entering the hollow waveguide. The PDL was then recorded as the difference between the maximum and minimum loss attainable by manipulating the polarization controller. The singlemode 3 μm core fibre was used with the 650 nm laser for these measurements as it was observed to be more stable than the 50 μm core fibre and 635 nm laser. The measured data is plotted along with the simulation predictions in Fig. 4.4. The measurements were in reasonable agreement with the simulation results for the 3 μm core fibre. A deviation of 0.2 dB corresponds to a difference of only 5%.

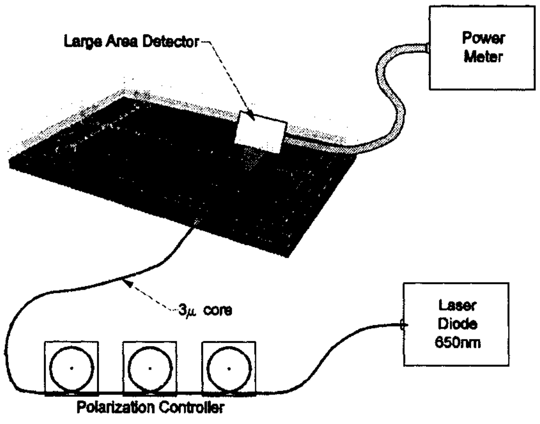

Figure 4.3: PDL measurement setup

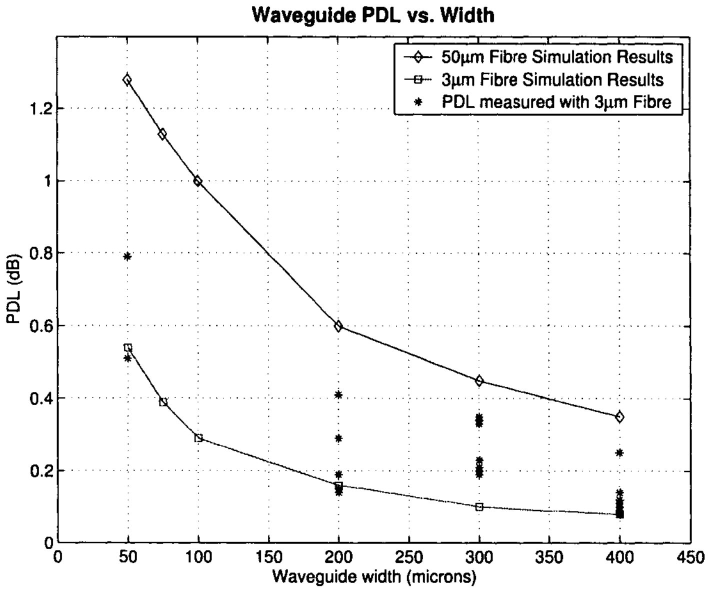

Figure 4.4: Measured PDL as a function of waveguide size

4.2 Fluorescence Detection Setup

In order to verify the devices described in this work are feasible for analyses involving fluorescent detection, the detection system shown in Fig. 4.5 was used. The setup used is the same as the one reported in Ref. [64] and [65] with a couple of modifications to improve sensitivity and ease of use.

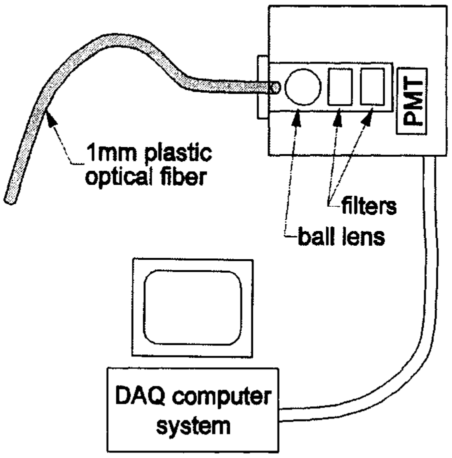

Figure 4.5: Fluorescence detection system

A large core (1 mm diameter) plastic optical fibre is used to guide light from the region of detection to a Hamamatsu R2949 photomultiplier tube (PMT). The high voltage required to operate the PMT is obtained via a Hamamatsu C6271 socket that the PMT is mounted in. The output voltage of the socket (which controls the gain of the PMT) is variable by means of another 0-10 V input. This input is computer controlled with an analog output from a National Instruments PCI-MIO-16E-4 data acquisition card (DAQ). The DAQ card is also used to record samples of the PMT output voltage at a rate of 10 kHz.

Before the light reaches the PMT it passes through a ball lens and filter assembly which blocks the laser light used for fluorescence excitation. The ball lens and filters are all 0.5" diameter and can be easily interchanged with other standard 0.5" optics.

4.2.1 Improvement of the Detection System

There were two modifications done to the PMT detection system. First, the PMT box and filter holder assembly were modified to minimize coupling loss to the PMT and allow access to the filters without opening the box. The distance from the PMT window to the end of the fibre was minimized so that more of the light diverging from the fibre would illuminate the PMT window directly. The filter holder assembly was also redesigned so that it could be screwed in from the outside of the box. This allowed for changing the filter configuration without opening the PMT box.

The second modification done to the detection system was the use of better filters to allow more fluorescence light to pass into the PMT. The old filters were passband filters centered at 710 nm. However, the fluorescence spectra is significantly wider than the passband of the filters. This unnecessarily eliminated the fluorescence above 725 nm. The replacement was chosen to be a Schott glass RG665 long pass filter which has a cutoff at 665 nm. Using this filter, the majority of the fluorescence above 665 nm should pass through to the PMT. See Fig. 4.6 for the spectral shape of the excitation laser, fluorescence and the two filters used.

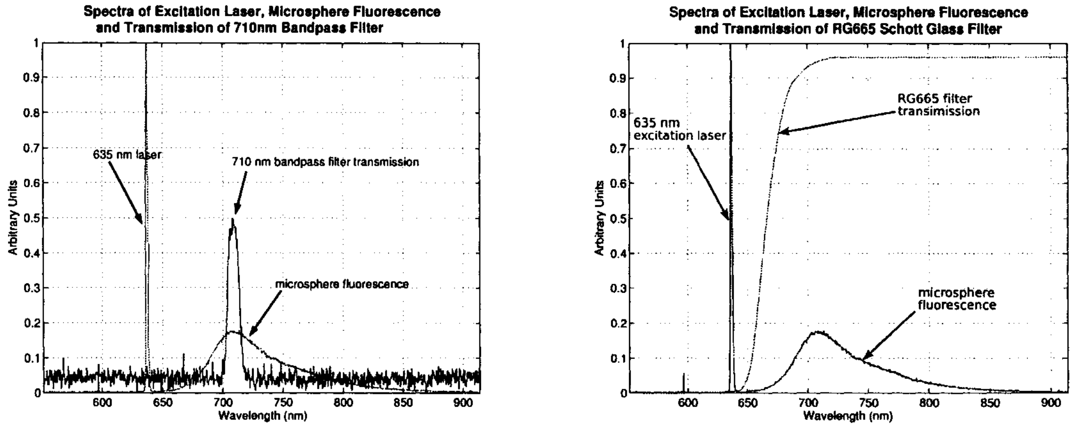

(a) Spectra for fluorescence detection using 710 nm bandpass filter

(b) Spectra for fluorescence detection using RG665 Schott glass filter

Figure 4.6: Comparison of fluorescent detection filters

A direct comparison of the detection system using the two different filter sets was undertaken. The results are shown in Fig. 4.7. This experiment was performed by illuminating a fluidic channel with the v-groove waveguides and detecting from overhead with a 1 mm plastic optical fibre. Fluorescence was collected as particles passed by and the PMT output signal was captured with the DAQ system. The filters were then replaced with the new RG665 filters and more data was gathered in the same fashion. Great care was taken to not disturb the physical setup of the chip and optical fibres when switching the filters.

From the data shown in Fig. 4.7 it can be seen that the signal-to-noise ratio (SNR) increased by a factor of 10. This increase in performance is attributed to the more complete transmission of the fluorescence signal as well as the improved peak transmittance of the new filters. The peak transmittance of the old 710 nm filters is just above 50%, while the peak transmittance of the new RG665 filters is above 95%.

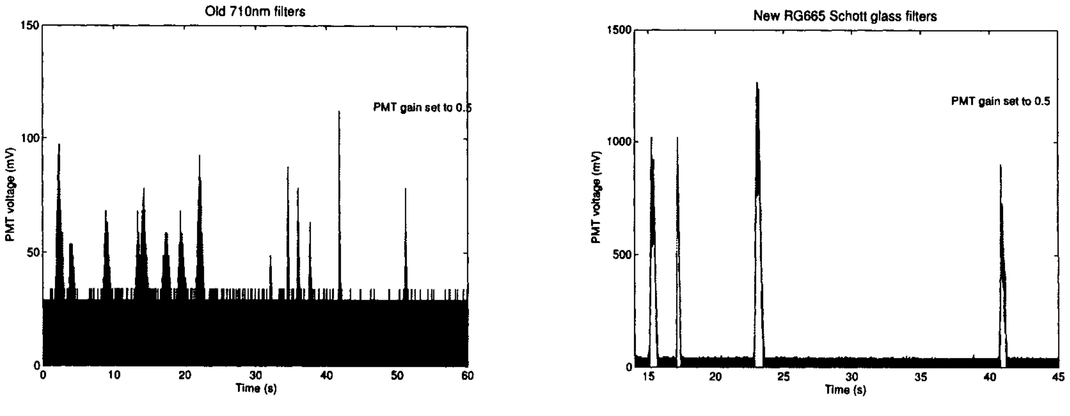

(a) 710nm passband filters

(b) Schott glass RG665

Figure 4.7: Evaluation of SNR with new filters

4.3 Detection of Fluorescent Microspheres

To simulate real world analysis in the biochip, fluorescent microspheres suspended in water were introduced into the microchannels. Fluid flow through the biochip was achieved by pressure driven flow as illustrated in Fig. 4.8. Fluid flows from the higher pressure reservoir (left side) to the lower pressure reservoir (right side). Since the size of the microchannels etched for these chips was relatively large (110 μm by 50 μm, roughly semi-circular), the velocity of the fluid flow in the center of the channel was sufficiently high for the purposes of this work (several mm/s). Due to the nature of the weak PDMS/pyrex bond, flow was initiated with a little bit of negative pressure. This was achieved by blocking the downstream reservoir and then pulling back on the syringe gently.

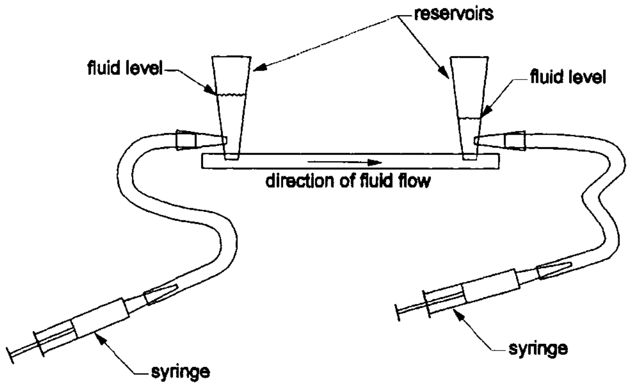

Figure 4.8: Controlling fluid flow with pressure

The fluid would not flow through the channel due to capillary action alone due to the hydrophobic surface chemistry of the PDMS.

The microspheres are made of polystyrene and have a fluorescent dye incorporated into them. They have a diameter of about 15 μm and are typically used to simulate cells due to their size. The microspheres used in this work were scarlet microspheres. According to the manufacturer [66], the absorption and emission peaks are at 651 nm and 680 nm respectively. These values describe the peak of the spectra curves and give no indication of the overall shape. Typical absorption and emission spectra are quite broad, see Fig. 1.1 for an example. The measured emission spectra for the microspheres used in these experiments are shown in Fig. 4.6.

The integrated optics of the biochip described in this work can be used in one of two ways. The v-groove waveguide and end facet can be used to direct light to the fluidic channel as a means of exciting fluorescence. Alternately, it can be used as a way of collecting fluorescence originating in the fluidic channel and guiding it to the edge of the chip. Both methods were successfully demonstrated.

Using the v-grooves as an excitation method worked with relatively little effort. Microspheres transported by pressure driven flow in the microchannels were illuminated by 635 nm light which was coupled into the hollow v-groove waveguide at the edge of the chip. The laser light excited fluorescence in the microspheres as they passed over the end facet of the v-groove waveguide. The emitted fluorescence was collected with a large plastic optical fibre and delivered to the PMT. The experimental setup and resulting PMT output signal is shown in Fig. 4.9.

By reversing the positions of the excitation and collection fibres, the end facet and hollow waveguide can be used to collect fluorescence. As shown in Fig. 4.10 (a), excitation light is directed at the region above the end facet with an optical fibre. Fluorescence from passing microspheres was then collected and guided to the edge of the chip where a large plastic optical fibre delivered it to the PMT. The resulting PMT output signal is shown in Fig. 4.10 (b). Using the v-grooves to detect fluorescence was not successful until the detection system was modified by replacing the 710 nm bandpass filters with the more efficient RG665 Schott glass filters as described in Sec. 4.2.1.

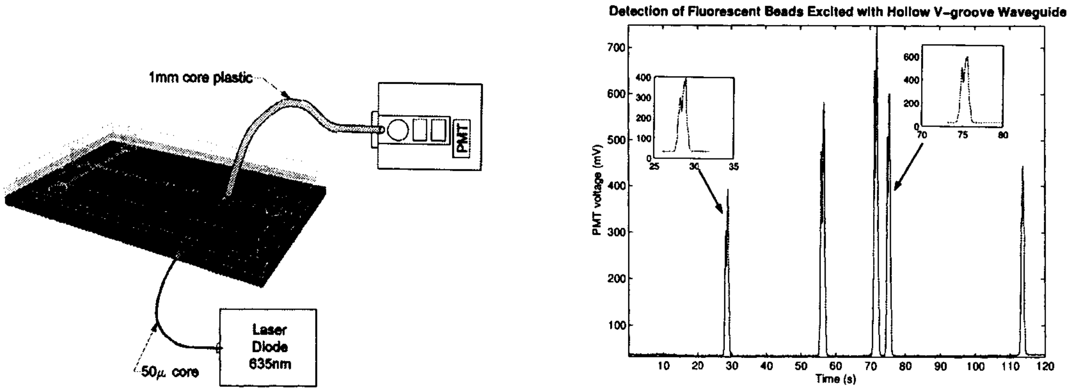

(a) Setup for using v-groove waveguides to excite fluorescence

(b) PMT signal from fluorescence excited by 635 nm light delivered by hollow v-groove waveguide

Figure 4.9: Detection of fluorescent microspheres using hollow v-groove waveguides for excitation

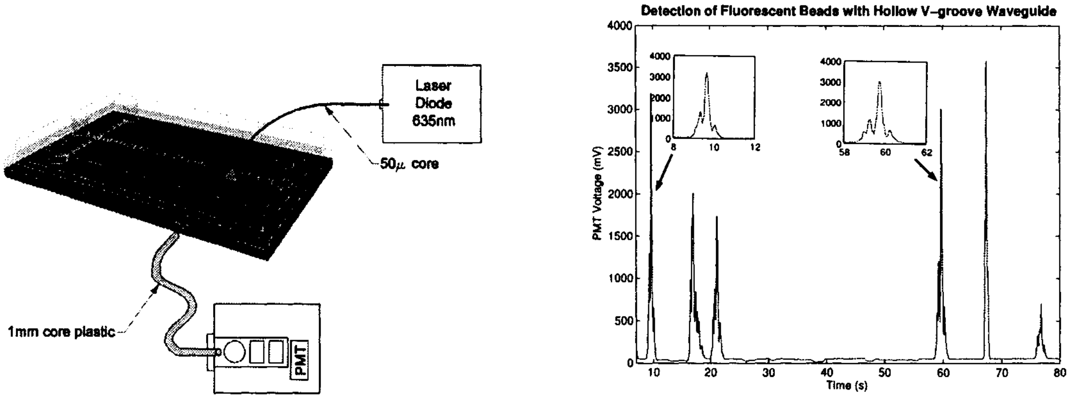

(a) Setup for using v-groove waveguides to collect fluorescence

(b) PMT signal from fluorescence collected by hollow v-groove waveguide

Figure 4.10: Detection of fluorescence using v-groove for collection

The structure of the fluorescence signal from the passing microspheres warrants further discussion. Looking at the insets of Fig. 4.9 (b) and Fig. 4.10 (b), it is interesting to note that the shape of the fluorescence signal from consecutive microspheres have similar shapes. The general shape of a peak caused by a passing microsphere remains consistent for a given illumination and collection geometry. This fluorescence signature is the result of the microsphere moving through the illumination profile combined with the response of the collection device. For example, in the experiment shown in Fig. 4.9, the illumination was delivered by the end facet and had a profile shape similar to Fig 2.13. As the microsphere passes through this illumination profile the fluorescence light emitted will be proportional to the strength of the excitation. At the same time the collection fibre was positioned at an angle to the surface of the chip in order to minimize direct illumination by the excitation light. The convolution of the illumination profile, collection geometry and moving microsphere all contribute to the multi-peak structure of the observed fluorescence signature. The two experiments, Fig. 4.9 and Fig. 4.10, obviously use different illumination and collection geometry and therefore differences in the fluorescence signature of passing beads can be expected.

The signature of a passing microsphere, if it were consistent, could be useful for velocity measurements similar to the concept reported in Ref. [67]. If the physical apparatus surrounding the chip were fixed to a particular geometry, it might be possible to calibrate the signature of the passing microsphere is order to gain information about its velocity.

Chapter 5

Conclusions

5.1 Summary of Work

The work detailed here can be seen as the initial foundation of a new type of hybrid silicon-glass biochip with integrated optics. This work demonstrated the feasibility of a multi-layer biochip with optics and fluidics in separate layers. Hollow metallized v-groove waveguides with reflective end facet were able to successfully guide light between the edge of the chip and the area of interest. The hollow waveguides were used both to guide excitation light as well as collect fluorescence emitted from microparticles.

Simulations of the metalized hollow waveguides were performed to predict the losses in this type of waveguide as well as understand the beam profile after reflection from the end-facet. The model can handle planar geometries with arbitrary complex index of refraction for each surface.

5.2 Future Work

In an attempt to direct future work on this project, the following issues should be addressed. There are several aspects of the fabrication process that could be improved. Refinement of the waveguide end facet position with respect to the fluidic channel is needed as well as corrections to mistakes in the mask set (undercutting of the KOH due to dicing lines and waveguide lines meeting to form a convex corner). Also, switching to a four mask process would decrease the amount of unneeded metal left on the silicon by using a separate mask instead of modifying mask #2. This excess metal was most likely the cause for the contact and anodic bonding failures.

Improving the bonding between the silicon and pyrex should also be a goal of further development. The quantity of waveguides on the chips should be reduced to leave more open space available for bonding. Also, a metal capable of withstanding anodic bonding temperatures should be investigated. Ti/Pt/Au has been suggested [68] as Pt is a good diffusion barrier. An alternate type of bonding that could also be investigated is eutectic bonding [52, p 392].

Another area of improvement is the thickness of the glass layer. Currently, the glass layer is about 500 μm thick. This was satisfactory for the initial work described here, but thinning this layer would improve the collection efficiency when the waveguides are used to gather fluorescence. It would also increase the amount of light that could be delivered to the fluidic channel if used for excitation. Purchasing thinner wafers, or thinning (chemically or mechanically) should be investigated as possible directions for this issue.

Determination of the best illumination angle of the fluidic channel which minimizes coupling to the waveguide. This should be done by simulation or experiment. Optimization of this illumination angle would help reduce the background noise when using the waveguide to collect fluorescence.

Advancement of the detection setup should also be considered. Specifically, investigating the use of a photo diode, or avalanche photo diode (APD) instead of the PMT as the optical sensor [20]. This would most likely not be an advancement in the limit of detection but would be a step toward a more robust hand-held type of detection system.

Attempting real-world analyses in these new biochips with collaboration with the Backhouse group should also be pursued. Both CE and RT-PCR should be achievable with current designs.

More integrated ways of delivering light to the fluidic channel in combination with hollow waveguides for collection could also be considered. For example, the excitation light could be delivered by a silver doped ion-exchange waveguide embedded in the pyrex. Collection of emitted fluorescence could then be done with the hollow waveguides. A project of this nature would involve a great deal of fabrication issues.

Silver should be investigated as the reflective metal as it has a higher reflectance than gold and is flatter through the visible region of the spectrum. The issue to be addressed is the degradation of the film reflectance due to oxidation. A passivation layer to prevent this oxidation could be investigated as a means of enabling the use of silver as the reflecting metal [44, 45].

The simulation model could be extended to deal with stratified dielectric layers on surfaces instead of only a single reflection coefficient. This would be useful for adding a protective layer (like AgBr, or AgI) over the silver to increase the reflectivity (instead of gold). The simulation software could also be extended to include curved surfaces.

This is a promising project with many avenues of possibility for future work.

Bibliography

[1] H. M. Widmer. Trends in industrial analytical chemistry. *TrAC Trends in Analytical Chemistry*, 2(1):VIII–X, 1983.

[2] A. Manz, N. Graber, and H. M. Widmer. Miniaturized total chemical analysis systems: A novel concept for chemical sensing. *Sensors and Actuators B: Chemical*, 1(1-6):244–248, 1990.

[3] J.W. Cooper, Yueju Wang, and C.S. Lee. Recent advances in capillary separations for proteomics. *Electrophoresis*, 25(23-24):3913 – 26, 2004.

[4] P. J. Obeid, T. K. Christopoulos, J. H. Crabtree, and C. J. Backhouse. Microfabricated device for DNA and RNA amplification by continuous-flow polymerase chain reaction and reverse transcription-polymerase chain reaction with cycle number selection. *Analytical Chemistry*, 75:288–295, 2003.

[5] G. H. W. Sanders and A. Manz. Chip-based microsystems for genomic and proteomic analysis. *TrAC Trends in Analytical Chemistry*, 19(6):364–378, 2000.

[6] R. Gómez, R. Bashir, A. Sarikaya, M.R. Ladisch, J. Sturgis, J.P. Robinson, T. Geng, A.K. Bhunia, H.L. Apple, and S. Wereley. Microfluidic biochip for impedance spectroscopy of biological species. *Biomedical Microdevices*, 3(3):201–209, 2001.

[7] S. Attiya, A. B. Jemere, T. Tang, G. Fitzpatrick, K. Seiler, N. Chiem, and D. J. Harrison. Design of an interface to allow microfluidic electrophoresis chips to drink from the fire hose of the external environment. *Electrophoresis*, 22(2):318–327, 2001.

[8] I. R. Lauks. Microfabricated biosensors and microanalytical systems for blood analysis. *Acc. Chem. Res.*, 31:317–324, 1998.

[9] J. Krüger, K. Singh, A. O'Neill, C. Jackson, A. Morrison, and P. O'Brien. Development of a microfluidic device for fluorescence activated cell sorting. *Journal of Micromechanics and Microengineering*, 12(4):486–494, 2002.

[10] J. Voldman, M. L. Gray, and M. A. Schmidt. Microfabrication in Biology and Medicine. *Annual Review of Biomedical Engineering*, 1(1):401–425, 1999.

[11] D. R. Reyes, D. Iossifidis, P. A. Auroux, and A. Manz. Micro total analysis systems. 1. introduction, theory, and technology. *Analytical Chemistry*, 74:2623–2636, 2002.

[12] P. A. Auroux, D. Iossifidis, D. R. Reyes, and A. Manz. Micro total analysis systems. 2. analytical standard operations and applications. *Analytical Chemistry*, 74:2637–2652, 2002.

[13] http://www.rsc.org/publishing/journals/lc/index.asp.

[14] http://www.iop.org/ej/journal/jmm.

[15] http://www.wiley-vch.de/publish/en/journals/alphabeticindex/2027/.

[16] http://pubs.acs.org/journals/ancham/.

[17] A. E. Kamholz. Proliferation of microfluidics in literature and intellectual property. *Lab on a Chip*, 4:16N, 2004.

[18] http://www.mcb.arizona.edu/ipc/fret/indexb.html.

[19] A. Giulietti, L. Overbergh, D. Valckx, B. Decallonne, R. Bouillon, and C. Mathieu. An overview of real-time quantitative PCR: Applications to quantify cytokine gene expression. *Methods*, 25:386–401, 2001.

[20] M. L. Chabinyc, D. T. Chiu, J. C. McDonald, A. D. Stroock, J. F. Christian, A. M. Karger, and G. M. Whitesides. An integrated fluorescence detection system in poly(dimethylsiloxane) for microfluidic applications. *Analytical Chemistry*, 73:4491–4498, 2001.

[21] http://www.micralyne.com.

[22] H. Qiao. Fabrication of biochips with integrated micro-optics and microfluidics. Master's thesis, University of Alberta, 2003.

[23] James N. McMullin. Laser fabrication of integrated microfluidic/micro-optic systems. In *Applications of Photonic Technology 4, Proceedings of the SPIE*, volume 4087, pages 1050–1055, 2000.

[24] K. B. Mogensen, A. El-Ali, J. Wolff, and J. P. Kutter. Integration of polymer waveguides for optical detection in microfabricated chemical analysis systems. *Applied Optics*, 42:4072–4079, 2003.

[25] P. Friis, K. Hoppe, O. Leistiko, K. B. Mogensen, J. Hübner, and Kutter J. P. Monolithic integration of microfluidic channels and optical waveguides in silica on silicon. *Applied Optics*, 40:6246–6251, 2001.

[26] N. J. Petersen, K. B. Mogensen, and J. P. Kutter. Performance of an in-plane detection cell with integrated waveguides for UV/Vis absorbance measurements on microfluidic seperation devices. *Electrophoresis*, 23:3528–3536, 2002.

[27] K. B. Mogensen, N. J. Petersen, J. Hübner, and J. P. Kutter. Monolithic integration of optical waveguides for absorbance detection in microfabricated electrophoresis devices. *Electrophoresis*, 22:3930–3938, 2001.

[28] J. C. McDonald, D. C. Duffy, J. R. Anderson, D. T. Chiu, H. Wu, O. J. A. Schueller, and G. M. Whitesides. Fabrication of microfluidic systems in poly(dimethylsiloxane). *Electrophoresis*, 21:21–40, 2000.

[29] J. M. K. Ng, I. Gitlin, A. D. Stroock, and G. M. Whitesides. Components for integrated poly(dimethylsiloxane) microfluidic systems. *Electrophoresis*, 23:3461–3473, 202.

[30] F. E. Lytle and B. G. Splawn. Performance of submillimeter square hollow waveguides. *Applied Optics*, 41:6660–6665, 2002.

[31] Y. Kikutani, A. Hibara, K. Uchiyama, H. Hisamoto, M. Toekshi, and T. Kitamori. Pile-up glass microreactor. *Lab on a Chip*, 2:193–196, 2002.

[32] J. B. Yoon, C. H. Han, E. Yoon, and C. K. Kim. Novel monolithic and multilevel integration of high-precision 3-d microfluidic components. *Proc. SPIE Int. Soc. Opt. Eng.*, 3515(1):183–191, 1998.

[33] R. S. Quake and A. Scherer. From Micro- to Nanofabrication with Soft Materials. *Science*, 290:1536–1540, Nov 2000.

[34] A. Daridon, V. Fascio, J. Lichtenberg, R. Wütrich, H. Langen, E. Verpoorte, and N. de Rooij. Multi-layer microfluidic glass chips for microanalytical applications. *Fresenius' Journal of Analytical Chemistry*, 371(2):261–269, 2001.

[35] J.-C. Roulet, R. Völkel, H.P. Herzig, E. Verpoorte, N.F. de Rooij, and R. Dändliker. Fabrication of multilayer systems combining microfluidic and microopticcal elements for fluorescence detection. *Microelectromechanical Systems, Journal of*, 10(4):482–491, 2001.

[36] J.-C. Roulet, R. Völkel, H.P. Herzig, E. Verpoorte, N.F. de Rooij, and R. Dändliker. Performance of an integrated microoptical system for fluorescence detection in microfluidic systems. *Analytical Chemistry*, 74:3400–3407, 2002.

[37] J.N. McMullin, R. Narendra, and C.R. James. Hollow metallic waveguides in silicon v-grooves. *Photonics Technology Letters, IEEE*, 5(9):1080–1082, 1993.

[38] D. J. Sadlery, M. J. Gartery, C. H. Ahny, S. Kohz, and A. L. Cook. Optical reflectivity of micromachined {111}-oriented silicon mirrors for optical input-output couplers. *Journal of Micromechanics and Microengineering*, 7:263–269, 1997.

[39] C. Strandman, L. Rosengren, H.G.A. Elderstig, and Y. Backlund. Fabrication of 45° mirrors together with well-defined v-grooves. *Microelectromechanical Systems, Journal of*, 4(4):213–219, 1995.

[40] R. M. Tiggelaar, T. T. Veenstra, R. G. P. Sanders, J. G. E. Gardeniers, M. C. Elwenspoek, and A. van den Berg. A light detection cell to be used in a micro analysis system for ammonia. *Talanta*, 56(2):331–339, 2002.

[41] M. A. Duguay, Y. Kokubun, T. L. Koch, and L. Pfeiffer. Antiresonant reflecting optical waveguides in SiO_2-Si multilayer structures. *Applied Physics Letters*, 49:13–15, 1986.

[42] H. Schmidt and D. Yin. Integrated arrow waveguides wth hollow cores. *Optics express*, 12:2710–2715, 2004.

[43] J. A. Harrington and C. C. Gregory. Hollow sapphire fibers for the delivery of CO_2 laser energy. *Optics Letters*, 15:541–543, 1990.

[44] J. A. Harrington. A review of IR transmitting, hollow waveguides. *Fiber and Integrated Optics*, 19:211–227, 2000.

[45] T. Wen, J. Gao, B. Bian, and J. Shen. Investigation on roughness of silver thin films inside silica capillaries for hollow waveguides. *Materials Letters*, 50(2-3):124–128, 2001.

[46] B.E.A. Saleh and M.C. Teich. *Fundamentals of Photonics*. John Wiley & Sons, 1991.

[47] Harland G. Tompkins. *Spectroscopic ellipsometry and reflectometry : a user's guide*. New York: Wiley, 1999.

[48] M. Born and E. Wolf. *Principles of optics : electromagnetic theory of propagation, interference and diffraction of light*. Pergamon Press, 6th ed. edition, 1980.

[49] E. Hecht. *Optics*. Addison-Wesley Publishing Company, 2nd. edition, 1990.

[50] J. E. Bresenham. Algorithm for computer control of a digital plotter. *IBM Systems Journal*, 4(1):25–30, 1965.

[51] G. T. A. Kovacs, N.I. Maluf, and K.E. Petersen. Bulk micromachining of silicon. In *Proceedings of the IEEE*, volume 86, pages 1536–1551, 1998.

[52] M. J. Madou. *Fundamentals of microfabrication : the science of miniaturization*. Boca Raton, Fla. : CRC Press, 2nd edition, 2002.

[53] K. Sato, M. Shikida, Y. Matsushima, T. Yamashiro, K. Asaumi, Y. Iriye, and M. Yamamoto. Characterization of orientation-dependent etching properties of single-crystal silicon: effects of KOH concentration. *Sensors and Actuators A: Physical*, 64(1):87–93, 1998.

[54] A. Hölke and H. T. Henderson. Ultra-deep anisotropic etching of (110) silicon. *Journal of Micromechanics and Microengineering*, 9(1):51–57, 1999.

[55] Private communication with Ken Westra, Director of University of Alberta NanoFab.

[56] J. B. Price. Anisotropic etching of silicon with KOH-H_2O-isopropyl alcohol. *Semiconductor Silicon, Second International Symposium on Silicon Materials Science and Technology*, 13-18:339–353, May 1973.

[57] E. Herr and H. Baltes. KOH etch rates of high-index planes from mechanically prepared silicon surfaces. *Solid-State Sensors and Actuators, Digest of Technical Papers, TRANSDUCERS '91*, 1:807–810, 1991.

[58] Private communication with Tiansheng Zhou, formerly of Micralyne.

[59] http://www.strataglass.us.

[60] Excerpt from Collin Twanow's thesis.

[61] E. D. Palik, editor. *Handbook of Optical Constants of Solids II*. Boston : Academic Press, 1991.

[62] U. Gösele Q.-Y. Tong. *Semiconductor wafer bonding : science and technology*. John Wiley & Sons, Inc, 1999.

[63] https://www.norlandprod.com/adhesives.html.

[64] J. N. McMullin, H. Qiao, S. Goel, and A. Grundmann. Optical detection system for biochips using plastic fiber optics. *Review of Scientific Instruments*, 74:4145–4149, September 2003.

[65] J. N. McMullin, H. Qiao, S. Goel, S. A. McColman, and A. Grundmann. Lab-on-a-chip optical detection system using plastic fiber optics. In *Applications of Photonic Technology 6, Proceedings of the SPIE*, volume 5260, pages 114–118, Dec 2003.

[66] http://probes.invitrogen.com/media/pis/mp08829.pdf.

[67] J. N. McMullin, H. Qiao, S. Goel, C. L. Ren, and D. Li. Integrated optical measurement of microfluid velocity. *Journal of Micromechanics and Microengineering*, 15:1810–1816, 2005.

[68] Private communication with Holly Rourke, Norcada Inc.

[69] http://www.oxy.com/oxychem/chemicals.htm.

Appendix A

Simulation Details

The simulation software is made up of five discrete programs. The general usage flow is shown in Fig. A.1.

The core of the simulation code is a MATLAB function called *reflect.* It takes the input rays, waveguide model, and optional output arguments and simulates the light propagation through the waveguide and saves the outputs requested by the user. The other programs, *WG_editor*, *ray_launcher*, *simulation_launcher* and *simulation_explorer* are friendly graphical user interfaces (GUIs) that make running and analysing the simulations less tedious.

WG_editor allows the user to create a waveguide model and save it in the form required by *reflect.* The program also attempts to display the waveguide model as it is created. Simple geometries are displayed well, but more complex geometries like a Si (111) end facet at the end of a V-groove are not handled as well. The coefficients of the waveguide planes are always what is saved as the model no matter how the program attempts to display it. The output plane, as well as the overall dimensions of the simulation space are defined as part of the waveguide model.

Ray_launcher is a GUI that enables the user to quickly generate a distribution of rays that is saved as an input file. The input file passes the starting locations, propagation vectors and power of each of the rays to be traced. In its current state, cartesian and radial geometries can be generated by *ray_launcher.*

Simulation_launcher is a simple GUI that writes a script to call *reflect* with the correct inputs and outputs so that the simulation runs as intended. This is needed due to the complexity of the parameters that can be passed into *reflect.* The main script that is generated can then be executed at a MATLAB shell to run the simulation.

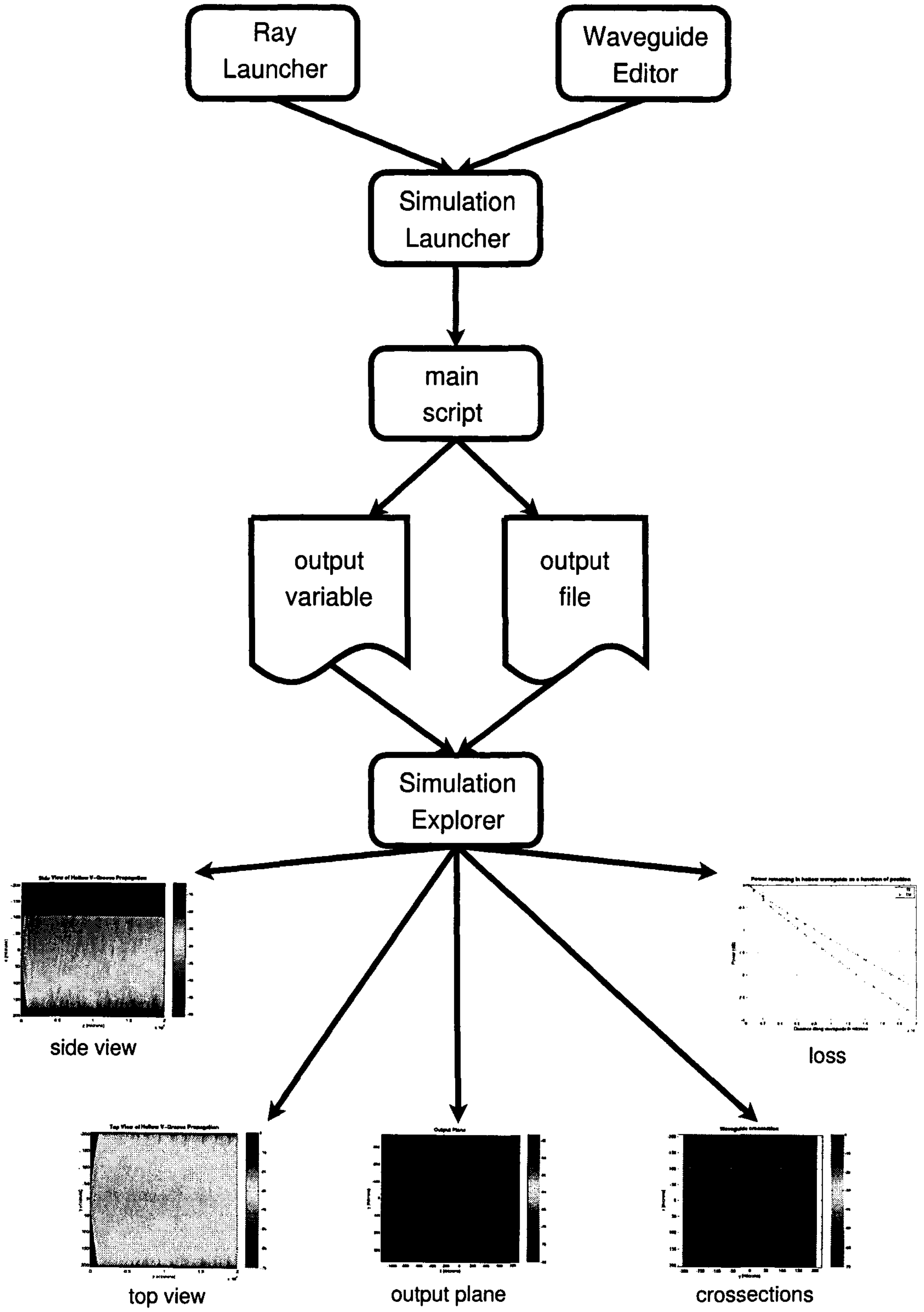

Figure A.1: Simulation software usage

The output files for each simulation are named according to a "run_id", which is specified by the user (using *simulation_launcher*). The outputs (crossections, top and side views) of the *reflect* code are saved in a MATLAB variable file, run_id.mat. The rays that intercept the output plane are recorded in a different output file, runid_out.dat. This output file can then be used as an input for a subsequent simulation as it has the same form as an input file.

Simulation_explorer provides a convenient way to quickly look at the output of a simulation. Simply clicking on a log file from a list in the GUI brings up the details of the simulation. There are also buttons to plot the side or top views, as well as the crossections and output plane.

Appendix B

Fabrication Details

Fabrication for this project was carried out at the University of Alberta NanoFab. The following is a step-by-step guide to fabricating the devices detailed in this work.

B.1 Fabrication of the Silicon Component

1. The fabrication of the silicon part of the device starts with a silicon wafer (500 μm thickness) with LPCVD nitride deposited on both sides. The wafers used for this work were purchased from Norcada. The original manufacturer was Strataglass [59].

2. HMDS

   Wafers are treated with HMDS vapour to improve adhesion of the resist. This step is done in the YES HMDS Oven. The procedure is completely automated and is a standard NanoFab process.

3. Spin Resist

   HPR504 resist is spin coated on the HMDS treated silicon wafers. The spread cycle is 500rpm for 10 seconds. Spin cycle is 4000rpm for 40 seconds.

4. Resist Soft Bake

   The freshly spun resist is soft baked on a Solitec vacuum hot plate at 110 degrees Celsius for 90 seconds. This is also a standard NanoFab process.

5. Mask Alignment and UV Exposure of the Pre-Etch Alignment Marks (mask #1)

   After the wafer has been allowed to cool, it is placed in the AB-M Contact Mask Aligner. The KOH etch mask (mask#1) is aligned to the wafer flat and brought into intimate contact with the wafer. All sections of the mask *except the pre-etch marks* were covered with black

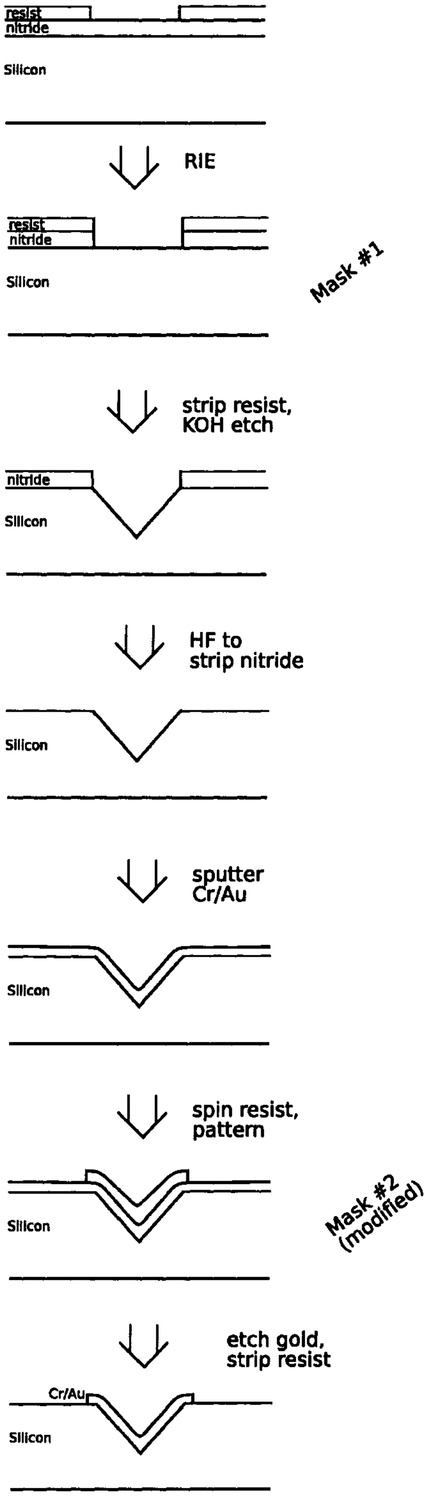

Figure B.1: Silicon fabrication process

tape in order to prevent exposure. The resist is then exposed with 435 nm UV light for approximately 3-4 seconds. The exposure time can be accurately calculated by determining the time to deliver 130 mJ/cm^2 of energy. The amount of time needed will depend on the power delivered by the UV light source. This information can be attained from the last routine calibration of the equipment. There is usually a notice detailing the results of the last calibration posted on the equipment.

6. Develop Photoresist

   The resist can then be developed using Shipley 354 developer. The develop time needed is approximately 18 seconds. The wafer should be checked to make sure all the resist is cleared from the desired features before proceeding.

7. RIE

   The hard mask is opened by a 90 second nitride etch in the Trion RIE. The standard nitride etch recipe stored in the Trion RIE was used to do the etch. The forward power was 125 W and the pressure was 150 mTorr. The gas flow rates were 45 sccm of CF_4 and 5 sccm O_2.

8. Strip Resist

   The HPR504 resist should now be stripped off by rinsing in acetone, then IPA, then DI water. The nitride layer with transferred mask features should now be exposed. The patterned nitride layer is the hard mask for the KOH etch.

9. KOH Pre-Etch

   The KOH etch is a time consuming step due to the etch bath warm-up time. A fresh batch of KOH should be mixed to 30% (w/w) and placed in the etch bath. See Appendix E for details on mixing KOH to a specific concentration. The temperature controller should be set to 105 $°C$ and the magnetic stirring turned on to about 2 Hz. The stirring helps to keep the temperature of the bath uniform. The bath will take approximately 2 hours to warm up to ~80 $°C$. The final temperature of the KOH bath may vary a bit depending on the ambient air temperature in the NanoFab. The reflux was column was not used to cover the KOH bath as it was suspected of contaminating the bath. A new KOH bath container was also used to alleviate concerns of contamination. The wafer is suspended in the KOH bath using a quartz holder. The wafer should be at an 45° angle (not vertical), as the hydrogen bubbles produced by the reaction more easily escape from the etched features. The etch time used for the pre-etch was 20 minutes. Once the etch is finished, the wafer should be removed from the etch bath and placed in a container of water for about 20 minutes. This helps to dissolve any reaction byproducts that may be left on the surface. The wafer should then be placed in the dump rinser for 5 cycles. This gave a depth of approximately 30 μm which was sufficient to easily see dislocations due to crystal misalignment in the pre-etch marks. The Tencor Alpha Step profilometer should be used to measure the exact etch depth of the features so that an etch rate can be determined.

10. Identify Crystal Planes

    Inspection of the pre-etch marks under a microscope should determine which trench is most aligned with the crystal planes. See Fig. 3.8 for an example of what to look for. This should be recorded and used later when aligning the mask for the next KOH etch step.

11. Repeat Steps 1 through 8

    The only difference is that the KOH etch mask is now entirely uncovered (no black tape). Also, the knowledge gained about the orientation of silicon crystal plane should be applied when aligning the mask this time. The pre-etch marks allow for easy alignment to within ~0.1 degrees.

12. KOH Etch of the V-grooves

    The etch time for the V-grooves is determined by the width of the widest feature. The geometry of the crystal defines what the the depth will be. To completely etch the 400 micron features to a 'v', a depth of 282 microns is required. With an etch rate of 1.3 μm/min, this will take approximately 220 minutes.

13. Strip the Nitride Mask

    Hydrofluoric acid (HF) was used to strip the nitride mask. Nitride etches very slowly, even in straight HF. All of the nitride should be removed after about 90 minutes.

14. Sputter Cr / Au

    The chrome / gold metal film is deposited using the Leskar two target sputter system. The deposition times are 3 minutes for the chrome and 9 minutes for the gold. This should deposit a film of about 30 nm of chrome and 75 nm of gold. The base pressure should be $1.8 * 10^{-6}$ Torr and the deposition pressure was 7.0 mTorr. The power applied to the chrome target and gold target is 300 W and 75 W respectively. These are standard parameters for Cr/Au deposition in the NanoFab.

15. Spin AZ4620 thick resist

    The metalized wafers are now spin coated with AZ4620 resist. A thick resist is needed as the deep v-groove feature can be a problem to cover. Spread speed of 300 rpm for 10 seconds, and spin speed of 1800 rpm for 25 seconds should give a resist thickness of about 12.5 μm.

16. Soft Bake thick resist and hydration

    The soft bake for AZ4620 is done on the CEE vacuum hot plate. The hot plate should be set at 100°C. With the nitrogen flow on, the wafer is placed on the hot plate for 90 seconds. Then the nitrogen flow is removed and the vacuum is applied for 60 seconds. The resist now needs to hydrate before it can be exposed. To accomplish this, it is placed in a box with a wet towel in the bottom for at least 2 hours.

17. Mask Alignment and UV exposure of the AZ4620 (mask #2)

    Mask #2 has to be modified by placing strips of black tape about 3 mm wide down the middle of each chip on the mask. This is so that when it is exposed, the resist over the all the v-groove end facets will remain. This modification is needed since mask #2 is also used for patterning the Cr/Au waveguide cap on the pyrex. The modified etch mask is now aligned to the alignment marks defined by the previous anisotropic etch and brought into contact with wafer. The resist should be exposed by 435 nm UV light for approximately 18 seconds. The required exposure energy dose is 1190 mJ/cm^2.

18. Develop the AZ4620 resist

    AZ4620 resist is developed with AK400 developer (diluted 4:1) for approximately 100 seconds. The wafer should be checked to make sure all the resist is cleared from the desired features before proceeding. It is also necessary to check if the resist completely covered over the corner of the v-grooves.

19. Au etch

    Gold is etched with hydroiodide acid and potassium iodide (this mixture is simply known as "gold etch"). The gold will turn black and then the chrome will start to show through. The etch time used was 37 seconds.

20. Cr etch

    Chrome etchant is ceric ammonium nitrate (commonly known as "chrome etch"). The chrome etch step is 30 seconds.

21. Spin AZ4620 resist for protective coating

    This step is purely a protective measure to minimize damage to the wafer surface during dicing of the chips. The same procedure was used as is described in steps 15 and 16.

B.2 Fabrication of the Pyrex Component

1. Start with Pyrex wafers that have a low-stress Cr/Au film on one side. The wafers used in this work were obtained from Micralyne as an in-kind contribution. Using Cr/Au sputtered films in the NanoFab as the mask for glass etch gives poor results as their is a high undercut rate due to the stress in the film.

2. Spin Resist

   The wafers are spin coated with HPR504 resist. The spread cycle is 500 rpm for 10 seconds. Spin cycle is 4000 rpm for 40 seconds.

3. Resist Soft Bake

   The freshly spun resist is soft baked in an oven for 30 minutes at $110°C$. This is a standard NanoFab process.

4. Mask Alignment and UV Exposure (mask #3)

   The resist covered wafer is now placed in the AB-M Contact Mask Aligner. The fluidic etch mask (mask #3) should be centered and brought into intimate contact with the wafer. The resist is exposed with 435 nm UV light for approximately 3-4 seconds.

5. Develop Photoresist

   The resist is developed using Shipley 354 developer. The develop time is approximately 18 seconds. The wafer should be checked to make sure all the resist is cleared from the desired features before proceeding.

6. Au Etch

   The gold etch step is 45 seconds. The details of this step are identical to step 19 in Appendix B.1.

7. Cr etch

   The chrome etch step is 25 seconds. The details of this step are identical to step 20 in Appendix B.1.

8. Glass etch

   Before the etch, the backside of the wafer should be protected from the etchant using blue tape. The etchant used was the 'Borofloat Etch' available in the NanoFab. The etch rate was measured to be 0.95 μm/min . The etch rate can vary with the ambient temperature in the clean room. To deal with this, the etch rate should be measured by doing a short 5 minute etch, measuring the etch rate (using the Alpha Step profilometer), then finishing the etch by calculating the time necessary to reach the desired depth. The channels should be etched to a depth of 50 μm.

9. Strip Resist

   Strip the HPR504 resist with an acetone, IPA, H_2O rinse.

10. Deposition of Cr/Au on the backside

    The chrome/gold metal film should be deposited on the backside of the pyrex wafer (opposite side from the etched fluidic channels) using the Leskar two target sputter system. In order to align the Cr/Au etch mask to the fluidic channels (in a subsequent step), it is necessary to leave areas over the glass etched alignment marks free of metal. To accomplish this, a permanent marker can be used where the Cr/Au is not meant to stick. The outer most wafer alignment marks should be colored over by permanent marker. See Appendix D for clarification. The deposition times were 3 minutes for the chrome, 9 minutes for the gold. This should deposit a film of about 30 nm of Chrome and 75 nm of gold. The base pressure was $1.8 * 10^{-6}$ Torr and the deposition pressure was 7.0 mTorr. The power applied to the chrome target was 300 W and 75 W to the gold.

11. Rinse off the metal over the alignment marks

    The metal that deposits over the permanent marker will lift off when rinsed with acetone and IPA. Gentle scrubbing with a soft foam sponge away from the center of the wafer can speed up the process.

12. Spin resist

    The backside of the wafers (side with newly deposited Cr/Au layer) are spin coated with HPR504 resist. The spread cycle is 500 rpm for 100 seconds. Spin cycle is 4000 rpm for 40 seconds.

13. Resist Soft Bake

    The freshly spun resist is soft baked in the oven at $110°C$ for 30 minutes. This is a standard NanoFab process.

14. Mask Alignment and UV Exposure (mask #2)

    The resist covered wafer is now placed in the AB-M Contact Mask Aligner. The Cr/Au etch mask (mask #2) is aligned to the pyrex etch alignment marks that are visible through the lifted-off regions of the Cr/Au metal film. Once aligned, the mask is brought into intimate contact with the wafer. The resist is exposed with 435 nm UV light for approximately 3-4 seconds.

15. Au Etch

    The etch time used was 45 seconds. This step is identical to step 6.

16. Cr etch

    The chrome etch step is 25 seconds. This step is identical to step 7.

17. Spin HPR504 resist for protective covering.

    Similar to step 21 of the previous section, this is a protective measure to minimize damage to the surface during dicing of the wafer. The resist should be spun on the patterned metal side of the wafer (not the glass etched side). The glass etched side will be protected by blue tape during dicing.

B.3 Dicing Details

To correct a mistake made on the mask design, 1 mm was cut off from the sides of both the silicon and the pyrex chips. The mistake was due to the dicing marks and the waveguide features resulting in a convex corner that was substantially undercut during the KOH etch.

A convex corner was left on the mask where the dicing lines met the v-grooves and substantial undercut resulted from exposed planes with high etch rates. To correct for this, the undercut section was simply cut off during dicing.

The chips have to be bonded individually to avoid leaving water and debris in the v-grooves during dicing.

B.4 Silicon / Pyrex Bonding Details

To bond the silicon and pyrex chips together, it is necessary to attach them to a larger substrate so they can be aligned using an AB-M mask aligner. The silicon chip was mounted to a blank silicon wafer by using a trace amount of water to adhere it. Similarly, the pyrex chip was mounted to a blank mask substrate (5" square glass plate) with a trace amount of water. The mask blank with the pyrex chip and the silicon wafer with chip were then loaded into the mask aligner. The pieces were brought together and aligned using the micropositioners. Once the alignment was good, the mask was raised and epoxy applied to the corners of the silicon chip. The mask was then lowered and the alignment of the chips fine-tuned as the pieces were brought into contact. Once the chips were in contact the epoxy was cured by exposing it with the UV lamp for 30 seconds.

B.5 PDMS Casting and Bonding

1. Clean a silicon wafer in piranha.
2. Treat silicon surface with HMDS in YES oven.
3. Mix the PDMS with 10 parts polymer, 1 part curing agent, for a total weight of 10 grams. This should give a PDMS thickness of 2 mm when cast over a wafer in the standard NanoFab PDMS apparatus.
4. Degas the PDMS for about 30 minutes in the PDMS vacuum/oven (with the oven off) or until there are no bubbles visible.
5. Place silicon wafer in the NanoFab PDMS jig and our the PDMS over the wafer. The standard NanoFab jig uses a rubber o-ring to contain the PDMS on top of the silicon wafer.
6. Cure in PDMS oven at 80°C for 2 hours.
7. Peel PDMS away from silicon wafer and immediately apply blue tape to the side of the PDMS that was in contact with the wafer. This is done to ensure the surface remains clean until it is ready to be bonded to the chip.
8. Cut PDMS into pieces that just fit inside the dimensions of the chip (leave the blue tape on during this procedure).
9. Punch fluid access holes with 1.5 mm diameter punch in the locations of the reservoirs (blue tape is still on). A plastic transparency can be used as a means of marking the locations of the holes.
10. Peel off tape and apply to the clean pyrex surface of the chip.

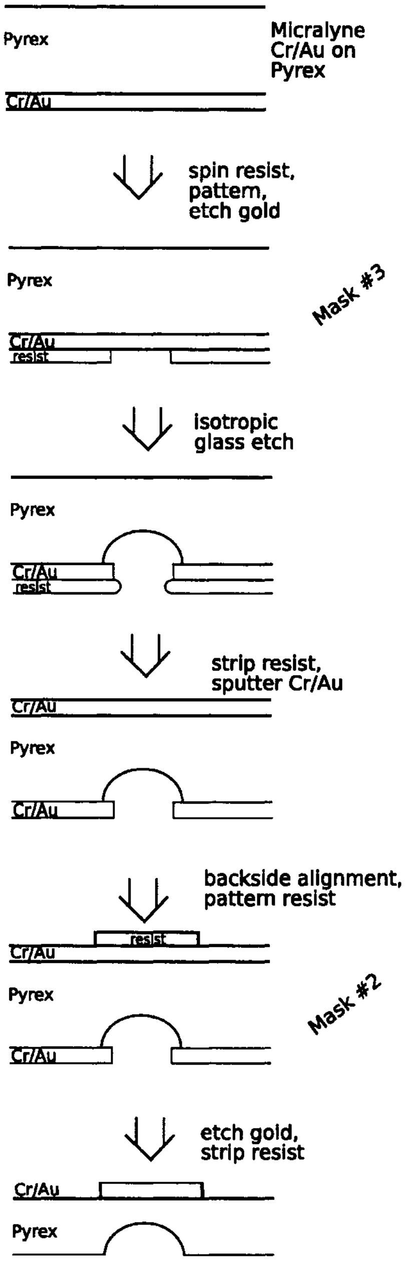

Figure B.2: Pyrex fabrication process

Appendix C

Geometry of Silicon V-Grooves

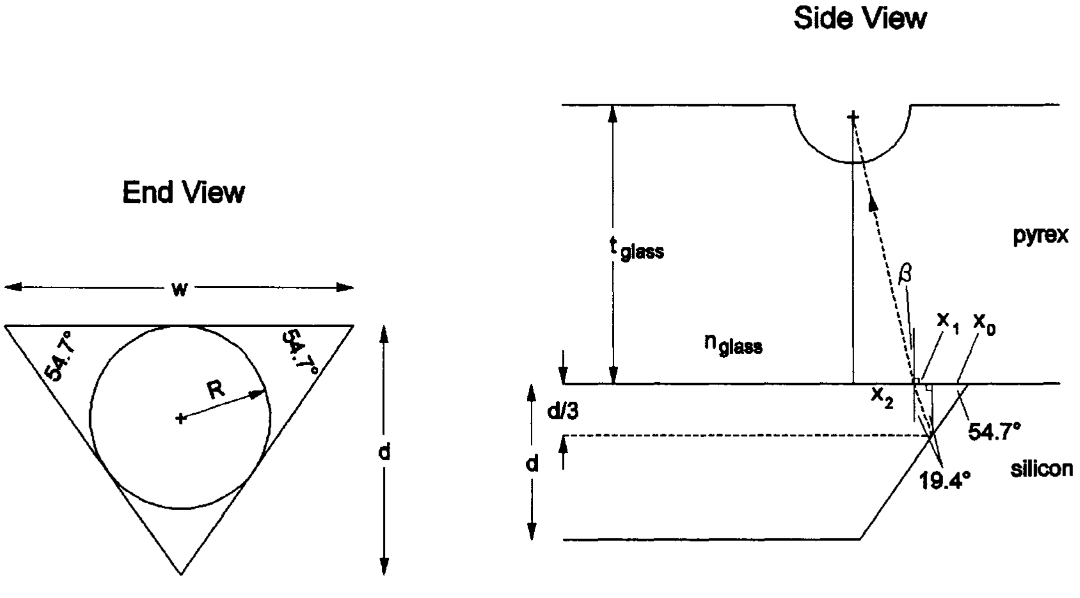

(a) end view of v-groove

(b) side view of v-groove with end-facet

Figure C.1: Silicon v-groove and end-facet geometry

$$d = \frac{w}{\sqrt{2}} \tag{C.1}$$

Given a width of an anisotropically etched silicon v-groove, Eq. C.1 is useful for calculating the depth.

$$R = \frac{w}{\sqrt{2}(1+\sqrt{3})} \tag{C.2}$$

Eq. C.2 calculates the maximum radius that will fit inside the v-groove. This is useful for determining if an optical fibre will couple efficiently into the hollow waveguide. See Fig C.1 (a).

$$x_0 = \frac{w}{6} \tag{C.3}$$

$$x_1 = \frac{w}{3\sqrt{2}} \tan(19.4^o) \tag{C.4}$$

$$x_2 = t_{glass} \frac{sin(19.4^o)}{\sqrt{n_{glass}^2 - \sin^2(19.4^o)}} \tag{C.5}$$

$$\beta = \arcsin\left(\frac{1}{n_{glass}} \sin(19.4^o)\right)$$

Eq. C.3 and C.4 assume that the power in the waveguide is uniformly distributed. A ray at the centroid of the waveguide will be a distance of d/3 down from top of the waveguide. See Fig. C.1 for clarification.

Appendix D

Mask Set Description

The current device fabrication process uses three masks. The complete mask set is shown in Fig. D.1. The light blue are glass etch features, the turquoise features are KOH etch and the yellow marks are what is to be left after the metal etch (Cr/Au). There are 4 separate chip designs on the mask, with 2 chips of each type.

There are two different alignment markings on the mask set. The KOH pre-etch marks are meant for aligning the KOH etch mask to the crystal plane of the silicon wafer. This is done after observing these pre-etch features under a microscope after a pre-etch step. The wafer and chip alignment marks are of the same type, but they serve different purposes. The wafer alignment marks are for aligning wafer to wafer steps (ie. glass etch to Cr/Au etch, step 14 from Appendix B.2). The chip alignment markings are needed during the bonding step.

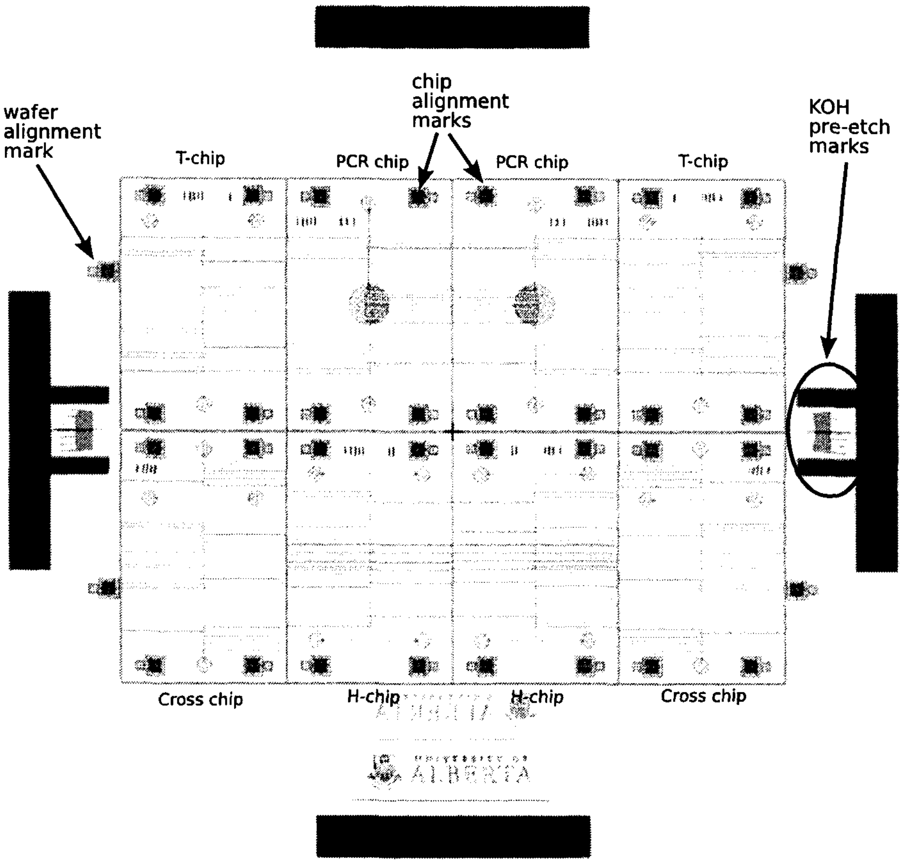

Figure D.1: Mask set

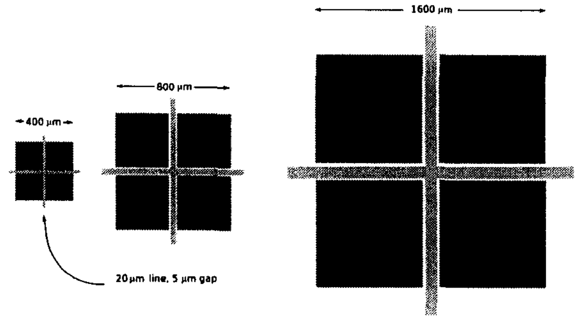

Figure D.2: Alignment marks

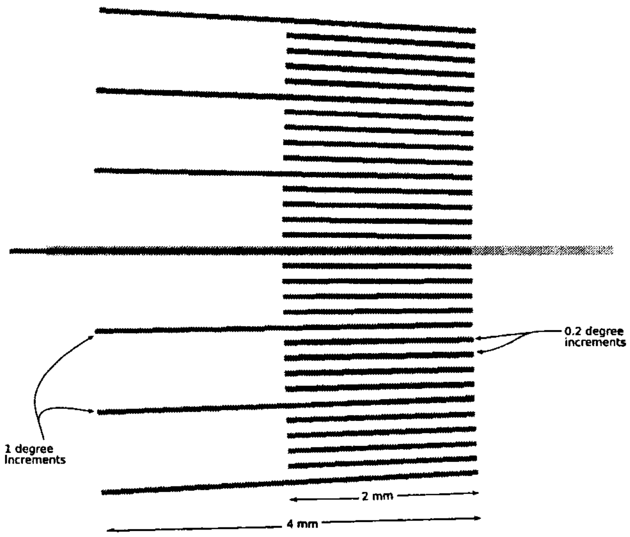

Figure D.3: Pre-etch marks

Appendix E

KOH Dilution Procedure

In general, KOH dilution is done by determining the volume of water to add so that the specific gravity of the final solution reaches a desired value. The final volume of the solution is not additive. Since KOH disassociates in water, you can not add the volume of the initial KOH to the volume of the water added to determine the solution final volume.

The specific gravity of KOH varies with %(w/w) as follows

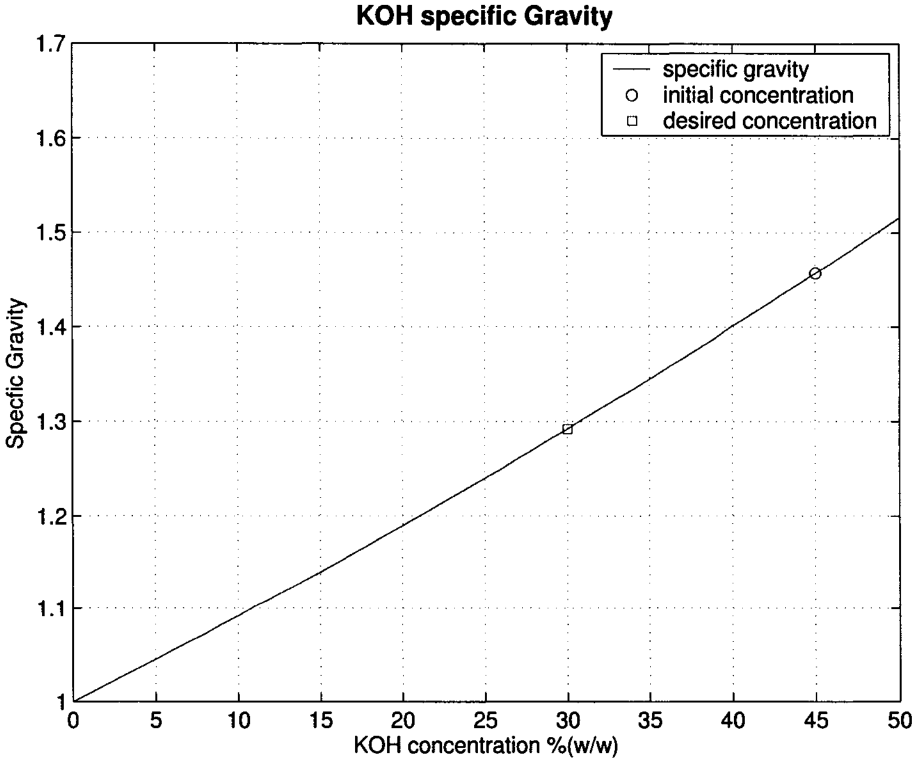

The formula used to calculate the volume of water added to achieve a particular concentration of KOH is as follows

$$V_{H_2O} = \frac{1000 \cdot SG_{desired}}{1 + (\frac{C_{desired}}{C_{initial} - C_{desired}})} \tag{E.1}$$

where $SG_{desired}$ is the specific gravity of the desired solution, $C_{desired}$ is the concentration in %(w/w) of the desired solution and $C_{initial}$ is the initial concentration of the KOH in %(w/w). This was modified from the dilution procedure given in the Caustic Potash Handbook from Occidental Petroleum Corporation [69].

In this work, a 30% (w/w) KOH solution was desired. The $SG_{desired}$ was 1.2880 for the desired concentration, $C_{desired}$ of 30% (w/w) KOH. The original solution available in the University of Alberta NanoFab had a concentration, $C_{initial}$ of 45% (w/w). The dilution procedure that was developed is as follows.

1. Pour 429 mL of water into a 1 L graduated cylinder.
2. Add 45% (w/w) KOH until the solution volume is 1 L.